Woodhead Publishing Series in Metals and Surface Engineering: Number 63

Underground pipeline corrosion

Detection, analysis and prevention

Edited by
Mark E. Orazem

ELSEVIER

AMSTERDAM • BOSTON • CAMBRIDGE • HEIDELBERG • LONDON
NEW YORK • OXFORD • PARIS • SAN DIEGO
SAN FRANCISCO • SINGAPORE • SYDNEY • TOKYO
Woodhead Publishing is an imprint of Elsevier

WP
WOODHEAD PUBLISHING

Woodhead Publishing is an imprint of Elsevier
80 High Street, Sawston, Cambridge, CB22 3HJ, UK
225 Wyman Street, Waltham, MA 02451, USA
Langford Lane, Kidlington, OX5 1GB, UK

British Library Cataloguing-in-Publication Data
A catalogue record for this book is available from the British Library

Library of Congress Control Number: 2013955405

ISBN 978-0-85709-509-1 (print)
ISBN 978-0-85709-926-6 (online)

For information on all Woodhead Publishing publications visit our website at http://store.elsevier.com/

Typeset by Newgen Knowledge Works Pvt Ltd, India

Printed and bound in the United Kingdom

4

Numerical simulations for cathodic protection of pipelines

C. LIU, A. SHANKAR and M. E. ORAZEM,
University of Florida, USA and D. P. RIEMER,
Hutchinson Technology, Inc., USA

DOI: 10.1533/9780857099266.1.85

Abstract: Mathematical models may be used for design or evaluation of cathodic protection (CP) systems. This chapter provides a historical perspective and a mathematical framework for the development of such models. The mathematical description accounts for calculation of both on- and off-potentials at arbitrarily located surfaces, thus making this approach attractive for simulation of external corrosion direct assessment (ECDA) methods. The approach also allows simulation of independent CP systems. Application of the model is presented for three cases: (a) enhancing interpretation of ECDA results in terms of the condition of the buried pipe; (b) simulating the detrimental influences of competing rectifier settings for crossing pipes protected by independent CP systems (e.g., rectifier wars); and (c) simulating the influence of coatings and coating holidays on the CP of above-ground tank bottoms.

Key words: cathodic protection, boundary element method (BEM), modeling, tank bottoms, external corrosion direct assessment (ECDA), close interval survey.

4.1 Introduction

While simple design equations may be used to predict the performance of corrosion mitigation strategies for simple geometries, more sophisticated numerical models are needed to account for the complexity of industrial structures. For example, the limited availability of right-of-way corridors requires that new pipelines be located next to existing pipelines. Placement of pipelines in close proximity introduces the potential for interference between systems providing CP to the respective pipelines. In addition, the modern use of coatings, introduced to lower the current requirement for CP of pipelines, introduces as well the potential for localized failure of pipes at discrete coating defects. The prediction of the performance of CP systems under these conditions requires a mathematical model that can account for

current and potential distributions in both angular and axial directions. The objective of this chapter is to provide a mathematical description of a model that accounts for CP of structures and to illustrate its application to some complex structures.

4.2 Historical perspective

The design of CP systems for pipelines is typically based on the use of anode resistance formulas (e.g., Dwight's and Sunde's equations), which were developed for bare copper grounding rods.[1,2] Under these conditions, the current density at the anode is much larger than that on the pipe, and resistance formulas, which ignore the current and potential distribution around the pipe, can be used. Newman presented semi-analytic design calculations that account for the potential distribution around the pipe under the assumption that damage to the coating could be considered as having reduced the uniform coating efficiency.[3]

Such analytic and semi-analytic approaches are not sufficiently general to allow all the possible configurations of pipes within a domain, the detailed treatment of potential variation within the pipes, and the polarization behavior of the metal surfaces.[4] Thus, numerical techniques are required. Of the available techniques, the boundary element method (BEM) is particularly attractive because it can provide accurate calculations for arbitrary geometries. The method solves only the governing equation on the boundaries, which is ideal for corrosion problems where all the activity takes place at the boundaries. Brebbia first applied the BEM for potential problems governed by Laplace's equation.[5] Aoki *et al*.[6] and Telles *et al*.[7] reported the first practical utilization of the BEM with simple nonlinear boundary conditions. Zamani and Chuang demonstrated optimization of cathodic current through adjustment of anode location.[8]

Brichau *et al*. first demonstrated the technique of coupling a finite element solution for pipe steel to a boundary element solution for the soil.[9] They also demonstrated stray current effects from electric railroad interference utilizing the same solution formulation.[10] However, their method was limited, in that it assumed that the potential and current distributions on the pipes and anodes were axisymmetric, allowing only axial variations. Aoki presented a similar technique that included optimization of anode locations and several soil conductivity changes for the case of a single pipe without angular variations in potential and current distributions.[11,12]

Kennelley *et al*.[13,14] used a 2-dimensional finite element model to address the influence of discrete coating holidays that exposed bare steel on otherwise well-coated pipes. This work allowed calculations for the angular potential and current distributions. A subsequent analysis employed boundary

elements to assess CP of a single pipe with discrete coating defects.[15,16] This work provided axial and angular potential and current distributions, but was limited to a short length of pipe.

Riemer and Orazem developed a solution for longer pipelines that accounted for the current and potential distributions both around the circumference and along the length of the pipe.[17] Their approach was used to evaluate the effectiveness of coupons used for assessing the level of CP applied to buried pipelines.[18] They also used the program to assess CP of tank bottoms.[19] Their development provides a foundation for modeling CP of long stretches of multiple pipelines, including interaction among CP networks, while retaining the flexibility to account for the role of discrete coating holidays. Adaptive integration techniques were used to generate values of sufficient accuracy for the terms appearing in the coefficient matrices. An efficient non-uniform meshing algorithm was used to avoid numerical errors associated with abrupt changes in mesh size while minimizing the computational cost of the program.

4.3 Model development

The model described below was originally designed to predict the performance of one or more CP systems for an arbitrary number of long pipelines with coating holidays (defects).[17] It has been applied as well for modeling the bottoms of storage tanks.[19] The external domain, e.g., soil or water, was assumed to have a uniform resistivity. Thus, concentrations of ionic species were assumed uniform. Heterogeneous reactions were assumed to occur only at boundaries to the domain of interest, and mass-transport or diffusion effects were included in the expressions for heterogeneous reactions.

4.3.1 Governing equations

The electrolyte conductivity was assumed to be uniform except perhaps at the boundaries. Thus, Laplace's equation governs potential in the electrolyte up to a thin boundary region surrounding the electrodes, i.e.,

$$\nabla^2 \Phi_{sol} = 0 \qquad [4.1]$$

where Φ_{sol} is the potential in the electrolyte referenced to some arbitrary reference electrode. In laminar flow, the boundary (Nernst diffusion layer) may be from 50 to 100 μm and the domain would be large compared to this dimension. For very long electrodes such as pipelines, or for high current densities such as plating, the resistance of the electrode materials and cur-

rent path cannot be neglected, and the potential distribution Φ_{met} within the electrode material can be found from

$$\nabla \cdot (\kappa_{met} \nabla \Phi_{met}) = 0 \quad [4.2]$$

where κ_{met} is the electrical conductivity of the electrode material and its connecting circuitry. Then the thermodynamic driving force for electrochemical reactions at the metal–soil interface can be written as

$$V = \Phi_{met} - \Phi_{sol} \quad [4.3]$$

The two domains, electrode materials and electrolytes, are linked through the electrode kinetics by the conversation of charge, which is expressed as

$$\kappa_{met} n \cdot \nabla \Phi_{met} = \kappa_{sol} n \cdot \nabla \Phi_{sol} \quad [4.4]$$

where κ_{sol} is the conductivity of the electrolyte,

$$\kappa_{sol} = F^2 \sum_i z_i^2 u_i c_i \quad [4.5]$$

F is the Faraday's constant, 96,485 C/eq, z_i is the charge of species i, u_i is the mobility of species i, and c_i is the concentration of species i.

4.3.2 Boundary conditions

To solve Equations [4.1] and [4.2], boundary conditions of the essential kind, ($\Phi = C_1$), or natural ($\vec{n} \cdot \nabla \Phi = C_2$) are needed for all the boundaries in the system (C_1 and C_2 may be constants or functions). For electrodes, the model accounts for polarization kinetics at bare metal and coated surfaces, and at anodes. Insulators may be treated as having a zero normal gradient, i.e., $\vec{n} \cdot \nabla \Phi = 0$, and the insulating nature of the electrolyte–air interface are accounted for through a method of reflections, which is shown later to be exact under the assumption that the interface is planar.

Bare electrode

Following Yan *et al.*,[20] the flux condition on bare metal was represented by a polarization curve that included electrode oxidation, oxygen reduction, and hydrogen evolution reactions, i.e.,

$$i = 10^{\frac{\Phi_{met}-\Phi_{sol}-E_{Fe}}{\beta_{Fe}}} - \left(\frac{1}{i_{lim,O_2}} + 10^{\frac{\Phi_{met}-\Phi_{sol}-E_{O_2}}{\beta_{O_2}}} \right)^{-1} - 10^{\frac{-(\Phi_{met}-\Phi_{sol}-E_{H_2})}{\beta_{H_2}}} \quad [4.6]$$

where Φ_{sol} is the potential in the electrolyte just above the metal,Φ_{met} is the potential of the metal at its surface, i_{lim,O_2} is the mass-transfer-limited current density for oxygen reduction. The parameters β_k and E_k represent the Tafel slope and effective equilibrium potential, respectively, for reaction k. The term E_k accounts for the concentration polarization, the equilibrium potential for the reversible reaction V_k, and the exchange-current-density $i_{o,k}$. If there is supporting electrolyte, then the error due to changes in concentration polarization will be small over a broad range of current densities. When compared to a Butler-Volmer equation, the functionality of E_k takes the form

$$E_k = -\beta_a \log i_o + V_o \quad [4.7]$$

where $V_o = \Phi_{met} - \Phi_{sol}$ is the potential difference such that the anodic and cathodic terms of the full Butler-Volmer equation for reaction k are equal and β_a is the anodic Tafel slope which takes the form

$$\beta_a = \frac{2.303RT}{\alpha_a nF} \quad [4.8]$$

Expressions similar to Equations [4.7] and [4.8] can be written for the cathodic terms in Equation [4.6]. Depending on the chemistry of the electrolyte, additional anodic and cathodic terms may be added to Equation [4.6].

Coated electrode

In order to model the current demands of coated materials, such as may be seen for a long coated pipeline, a model for the polarization of a coated electrode was used. The coating was assumed to act both as a highly resistive electronic conductor and as a barrier to mass-transport. Corrosion, oxygen reduction, and hydrogen evolution reactions were assumed to take place under the coating. The potential drop through the film or coating was expressed as[15]

$$i = \frac{\Phi_{sol} - \Phi_{in}}{\rho\delta} \quad [4.9]$$

where Φ_{sol} is the potential in the electrolyte next to the coating, Φ_{in} is the potential at the underside of the coating just above the steel, ρ is the resistivity of the coating and δ is the thickness of the coating. Thus,

$$i = \frac{A_{pore}}{A}\left[10^{\frac{\Phi_{met}-\Phi_{in}-\Phi_{Fe}}{\beta_{Fe}}} - \left(\frac{1}{(1-\alpha_{Block})i_{lim,O_2}} + 10^{\frac{\Phi_{met}-\Phi_{in}-\Phi_{0_2}}{\beta_{0_2}}}\right)^{-1} - 10^{\frac{-(\Phi_{met}-\Phi_{in}-\Phi_{H_2})}{\beta_{H_2}}}\right] \quad [4.10]$$

where A_{pore}/A is the effective surface area available for reactions, and α_{Block} accounts for reduced transport of oxygen through the barrier. The coating was assumed to have absorbed sufficient water to ensure that the hydrogen reaction was not mass-transfer limited within the effective surface area. Equation (4.9) and (4.10) were solved simultaneously to eliminate Φ_{in} and relate Φ_{sol} to i.

Anodes

To account for potential draw-down at the anode, the flux condition at the anode employed a simple polarization model accounting for corrosion and oxygen reduction as

$$i = i_{O_2}\left(10^{\frac{\Phi_{met}-\Phi_{sol}-E_{corr}}{\beta_{anode}}} - 1\right) \quad [4.11]$$

where i_{O_2} is the mass-transfer-limited current density for oxygen reduction, E_{Corr} is the free corrosion potential of the anode and β is the Tafel slope for the anode corrosion reaction. Typical parameter values are given in the literature.[19,21] In order to have the necessary essential boundary conditions, Equation [4.11] was solved for Φ_{sol}, whereas Equations [4.6]–[4.10] were used as natural boundary conditions on the cathodes.

4.3.3 Numerical solution

Equation [4.1] was solved using the boundary integral method (BIM),[22] which takes the form

$$\Phi_i + \int_\Gamma \Phi\left(\frac{\partial G(\xi,x)}{\partial \vec{n}}\right)d\Gamma(x) = \int_\Gamma G(\xi,x)(\vec{n}\cdot\nabla\Phi)d\Gamma(x) \quad [4.12]$$

valid for any point i within a domain Ω, where Γ represents surfaces of electrodes and insulators and $G(\xi,x)$ is the Green's function for Laplace's equation. G relates to a source point $\xi = (x_o, y_o, z_o)$ and field point $x = (x, y, z)$ by

$$G(\xi, x) = \frac{1}{4\pi r(\xi, x)} \quad [4.13]$$

where r is defined as

$$r(\xi, x) = \sqrt{(x - x_o)^2 + (y - y_o)^2 + (z - z_o)^2} \quad [4.14]$$

Equation [4.12] is exact for any domain Ω with surface $\partial G = \Gamma$. Error will come from discretizing Equation [4.12] into a boundary element method (BEM).

When the source point i is moved to a boundary, both integrals will have a singularity at i and the quantity Φ_i appears in two places

$$c_i \Phi_i + \int_\Gamma \Phi \left(\frac{\partial G(\xi, x)}{\partial \vec{n}} \right) d\Gamma(x) = \int_\Gamma G(\xi, x)(\vec{n} \cdot \nabla \Phi) d\Gamma(x) \quad [4.15]$$

where c_i now represents the solid angle of the surface Γ at the source point, and a second order singularity appears in the first integral. It has a finite value that can be quickly shown by transforming the integral to spherical coordinates with origin i.

Half-space

In the present work, it is assumed that the domain of the electrolyte can be accounted for as a half-space with a planar boundary described by the equation $z_o = 0$. A specialization of the Green's function is used to account exactly for there being only a half-space. It is derived using the method of images[23] and takes the form

$$G_{\xi,x} = -\frac{1}{r(x_i, x_j)} - \frac{1}{r(x_i, x_j')} \quad [4.16]$$

where, as is shown in Fig. 4.1, x_j' is the reflected field point about the plane that defines the half-space, $z_o = 0$. The derivative of G with respect to the unit normal vector at the field point is

$$4\pi \frac{\partial G_{i,j}}{\partial \vec{n}} = -\vec{n}_{\mathbf{x}_j} \cdot \nabla \frac{1}{r} - \vec{n}_{\mathbf{x}_j'} \cdot \nabla \frac{1}{r'} \quad [4.17]$$

which becomes the kernel of the first integral in Equation [4.15]. At a source point on the plane of reflection, the flux in the z-direction is equal to zero. It can be verified by taking the z-component of the gradient of Equations [4.16] and [4.17] at a source point given by $\mathbf{x}_o = [x_o, y_o, z_o = 0]$

$$4\pi \frac{\partial G}{\partial z_0}\bigg|_{z_o=0} = \frac{z}{r^3} - \frac{z}{r'^3} = 0 \qquad [4.18]$$

and for the normal derivative

$$4\pi \frac{\partial}{\partial z_o}\left(\frac{\partial G}{\partial \vec{n}}\right)\bigg|_{z_o=0} = \frac{-3z^2\vec{n}_z}{r^5} + \frac{3z^2\vec{n}_z}{r'^5} - \frac{\vec{n}_z}{r'^3} + \frac{\vec{n}_z}{r^3} = 0 \qquad [4.19]$$

because at $z = 0, r = r'$.

An equation of the form of Equation [4.15] was written for each node in the mesh describing the surfaces of the components of an electrolytic system, i.e. anodes, cathodes, and insulators not accounted for through the Green's function.

The final surface to account for is the hemisphere at an infinite distance that encloses the system. The surface is assumed to have a single unknown potential, Φ_∞, and no current passes through it. One more term is added to the left hand side of Equation [4.15], which is the integral of $\Phi_\infty\left(\vec{n}\cdot\nabla G_{i,j}\right)$ over the surface of the enclosing hemisphere of the half-space. The outward normal vector to the enclosing surface centered at $x_j = (x_0, y_0, z_0)$ at the integration point $x_i = (x, y, z)$ is in the same direction as the line-segment r and of unit length and given by

$$\vec{n} = \frac{1}{r}[(x - x_o), (y - y_o), (z - z_o)] \qquad [4.20]$$

The integral can be calculated by a transformation to spherical coordinates:

$$\lim_{\rho\to\infty} \int_0^{2\pi} \int_0^{\pi/2} \Phi_\infty \left(\vec{n}\cdot\nabla G_{i,j}\right) \rho^2 \sin\phi \, \mathrm{d}\phi \, \mathrm{d}\theta \qquad [4.21]$$

For any point on the plane $z = 0$, Equation [4.21] is calculated to be identically equal to 1 for the Green's function given in Equation [4.16]. The term on the left hand side of Equation [4.15] is equal to 0 since no current crosses

the surface. Because of the additional unknown, one more equation must be added that explicitly states the conservation of charge on the remaining surfaces, i.e.,

$$0 = \int_{\Gamma} \vec{n} \cdot \nabla \Phi_{\text{sol}} d\Gamma \qquad [4.22]$$

Equation [4.2], which governs the current flow within the materials of the cathode, anode, and connecting circuitry, was solved using a finite element method (FEM) in three dimensions. The same mesh used for the BEM solution in the electrolyte domain was used for the FEM solution in the electrode material domain under the assumption that the electrode was a thin annulus with negligible potential variation within the thickness of the material. The two methods were coupled by Equation [4.4], which provides a charge balance at the interface. The equation is also equal to the kinetic expressions in Equations [4.6] and [4.9]–[4.11] scaled by the conductivity, i.e.,

$$\vec{n} \cdot \nabla \Phi_{\text{sol}} = -\frac{i_{\text{kinetics}}}{\kappa_{\text{sol}}} \qquad [4.23]$$

or

$$\vec{n} \cdot \nabla \Phi_{\text{met}} = -\frac{i_{\text{kinetics}}}{\kappa_{\text{met}}} \qquad [4.24]$$

for the non-electrolyte portion of the circuit. Pipelines and anodes were joined in the non-electrolyte circuit through use of 1-D finite elements of appropriate resistance.

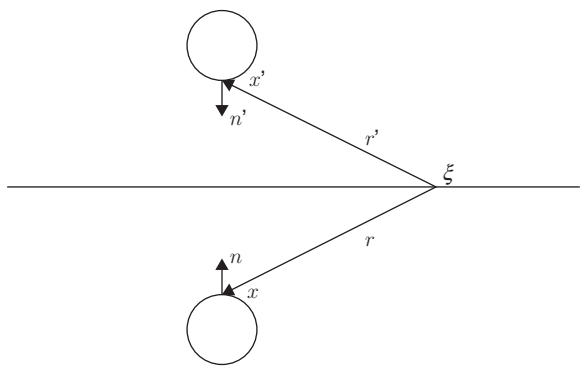

4.1 Diagram of source field and image of field.

Solving the nonlinear system

A variable transformation, $\Psi = \Phi_{met} - \Phi_{sol}$ was needed to provide stable convergence behavior for the combined BEM and FEM system of equations. Here, Ψ represents the driving force for the electrochemical kinetics. The variable Φ_{met} was eliminated from the system of equations and, upon adding the necessary terms for the potential at infinity and charge conversation, the system of equations could be written as

$$\begin{bmatrix} 0 & -G_{a,c} & H_{c,c} & H_{a,c} & -4\pi \\ 0 & -G_{a,a} & H_{c,a} & H_{a,a} & -4\pi \\ K_c & 0 & K_c & 0 & 0 \\ 0 & -\widehat{F}_a & 0 & K_a & 0 \\ 0 & -A_a & 0 & 0 & 0 \end{bmatrix} \begin{bmatrix} \Psi_c \\ \vec{n}\cdot\nabla\Phi_a \\ \Phi_c \\ \Phi_a \\ \Phi_\infty \end{bmatrix} = \begin{bmatrix} G_{c,c} & 0 \\ G_{c,a} & 0 \\ \widehat{F}_c & 0 \\ 0 & -K_a \\ A_c & 0 \end{bmatrix} \begin{bmatrix} \vec{n}\cdot\nabla\Phi_c \\ \Psi_a \end{bmatrix} \qquad [4.25]$$

where all of the unknowns have been moved to the left hand side and all the Φ terms refer to the potential in the electrolyte next to an electrode. The terms H and G are sub-matrices resulting from evaluation of the integrals in Equation [4.15]. Following the matrix notation of Brebbia *et al.*,[22] the first subscript to appear is the field point and the second is the source point. The sub-matrix K is the stiffness matrix from the FEM solution for the electrode materials and $\widehat{F}$ is the charge balance between the electrode and electrolyte domains. The sub-matrix A, given by

$$A = \int_{-1}^{1} \xi(\Gamma)\eta(\Gamma)J \, \mathrm{d}\Gamma \qquad [4.26]$$

is the surface area as represented by the shape functions for the elements used. The term J is the Jacobian of the coordinate transformations from Cartesian to curvilinear. It provides the correct weighting of the nodal values of the current density such that electroneutrality is enforced.

4.3.4 Calculation of potentials within the electrolyte

The model allows calculation of both on- and off-potentials at arbitrarily chosen locations within the electrolyte or on the electrolyte surface defined by the Green's function through the method of the images. The on-potential is defined as the potential that would be measured between a reference electrode at some point in the electrolyte and a cathode if the anodes were connected to the cathodes and current were flowing between them. The off-potential is defined as the potential difference measured between a

reference electrode at some point within the electrolyte and the cathode at a moment just after the anodes have been disconnected but the cathodes are still polarized. The method employed is summarized below.

On-potentials

The on-potential was obtained under the conditions where anodes are connected to the cathodes and, in the case of impressed current systems, are energized. The condition is straightforward to model. Using the solution for the entire electrolytic systems, points in the domains were calculated using equations described by Brebbia *et al*:[22]

$$\Phi_{\mathrm{i}} = \int_{\Gamma} G_{\mathrm{i,j}}(\vec{n}\cdot\nabla\Phi)\,\mathrm{d}\Gamma - \int_{\Gamma}\Phi(\vec{n}\cdot\nabla G_{\mathrm{i,j}})\,\mathrm{d}\Gamma \qquad [4.27]$$

where Φ_i is the unknown potential at a point not on the boundary Γ, and Φ and $\vec{n}\cdot\nabla\Phi$ are the solutions on Γ found by solving Equation [4.17].

Current density vectors can be found by differentiating Equation [4.27] at the source points.

$$\frac{\partial\Phi_{\mathrm{i}}}{\partial x_{\ell}} = \int_{\Gamma}\frac{\partial G_{\mathrm{i,j}}}{\partial x_{\ell}}(\vec{n}\cdot\nabla\Phi)\mathrm{d}\Gamma - \int_{\Gamma}\Phi\frac{\partial(\vec{n}\cdot\nabla G_{\mathrm{i,j}})}{\partial x_{\ell}}\,\mathrm{d}\Gamma \qquad [4.28]$$

where three equations of the form of Equation [4.28] are written for the three components of the current vector, $\ell = 1, 2, 3$. The resulting gradient of Φ_i is combined with the electrolyte conductivity to get the current.

Off-potentials

Off-potentials were calculated after a solution was obtained using the model described above. The anodes were removed from the problem, and the calculated potentials on the cathode were used as boundary conditions for a new calculation. As the metal under the coating is polarized and, therefore, the source of the potential, the potential used for coated electrodes was the value underneath the coating, Φ_{in} (see Equations [4.9] and [4.10]).

Equation [4.25] was rewritten dropping the anodes and using the previous solution for the potential on the cathodes as the known boundary condition, i.e.,

$$\begin{bmatrix} H_{\mathrm{p,p}} & -4\pi \\ 0 & 0 \end{bmatrix}\begin{bmatrix} \Phi_{\mathrm{in,p}} \\ \Phi_{\infty} \end{bmatrix} = \begin{bmatrix} G_{\mathrm{p,p}} \\ A_{\mathrm{p}} \end{bmatrix}\begin{bmatrix} \vec{n}\cdot\nabla\Phi_{\mathrm{in,p}} \end{bmatrix} \qquad [4.29]$$

where a new potential at infinity, Φ_∞, is found. All the values on the left hand side of Equation [4.29] are known, and the current densities, driven by the potential distribution along the cathodes, can be easily found. The new solution is then used to find the potentials within the electrolyte through Equation [4.12] using only the previous cathodes as sources.

4.4 Model validation

A computer code was written that implements the above model. The model can be compared to analytical solutions to Laplace's equation to validate the code.

4.4.1 Comparison to analytic solutions

The first comparison was made to the variation of potential around a disk electrode placed at the surface of a semi-infinite electrolyte with a hemispherical counter electrode infinitely far away. An analytic solution by Newman is available.[24] A limitation of the numerical model as implemented was that all anodes/cathodes had to be either disks or cylinders. A simple remedy would be to make the potential at infinity (Φ_∞) a known, and move it to the other side of Equation [4.17]. Then the new unknown is the total current entering or leaving the system through the hemisphere at infinity that encloses the system. In the case presented here, a counter electrode that was a factor of 4.0×10^{11} times larger than the disk was used to approximate the counter electrode in Newman's example. It was moved as far from the disk as numerically practicable.

A number of points were selected on the electrolyte surface for calculation of the potential. To illustrate the procedure, a grid of points extending away from the disk is presented in Fig. 4.2 where a calculation would be performed at each line intersection. The center section of points oriented in the r direction is used for comparison.

A comparison between the numerical and analytical results is presented in Fig. 4.3. The values of potential are in good agreement, and the error

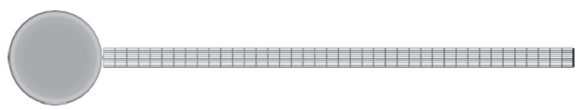

4.2 Completed mesh with points for soil surface potential calculation added. The points are represented as a grid where the intersections of the lines are the calculation points.

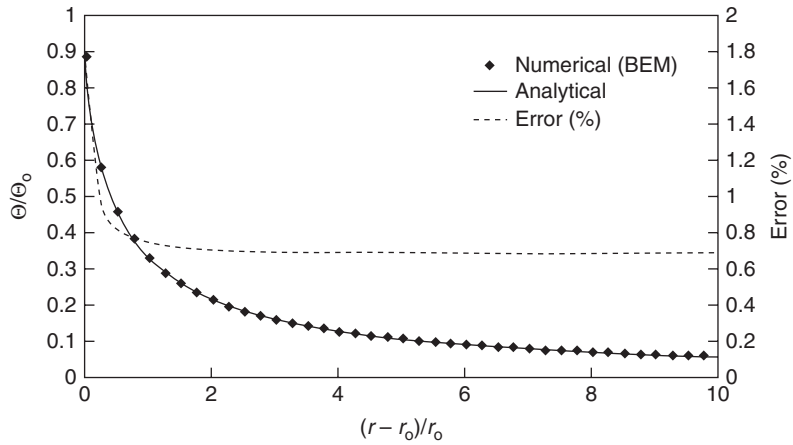

4.3 Comparison of the analytical and numerical solutions for the potential at the electrolyte surface. The term represents the distance from the edge of the disk.

between the analytical and numerical solutions is less than 1.8%. The increase in error close to the disk is the due to the fact that the numerical method cannot adequately represent the infinite current density at the edge of the disk. The constant error of 0.7% far from the disk is due to the finite size of the counter electrode and decreases as the counter-electrode area is increased.

A second validation was done against Kasper's solution for parallel cylinders of unequal size.[25] In this case, two cylinders were placed far from the electrolyte surface. One was 0.5 m diameter, the second was 0.1 m diameter, and they were placed such that their centers were 1 m apart as presented in Fig. 4.4. The boundary conditions for both surfaces were equipotential with the first set to 0 V and the second set to 1 V.

The potential in the electrolyte was calculated for a line running from the large cylinder to the small. The result is compared to the analytic solution in Fig. 4.5. The error in the numerical method does not exceed 0.1%. Therefore, given any arbitrary current and potential distribution on a set of electrodes that satisfies Laplace's equation, the resulting potential distribution within the electrolyte can be calculated with reasonable accuracy.

If the potential calculated at some point in the electrolyte is subtracted from another point at an electrode surface, one would have a reasonable approximation of a physical measurement made with a reference electrode. Therefore, the numerical method may be used to evaluate ways of using reference electrodes to determine the condition of an electrolytic system, such as a CP system or solid phase electrolytes.

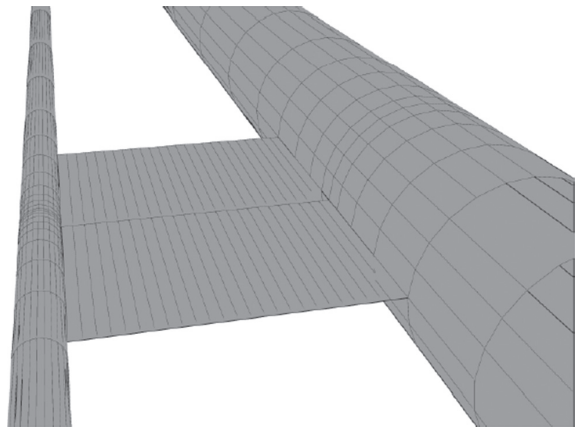

4.4 Model used to compare numerical method to Kasper's solution for two parallel cylinders. The surface between the cylinders represents the points in the electrolyte to calculate the potential.

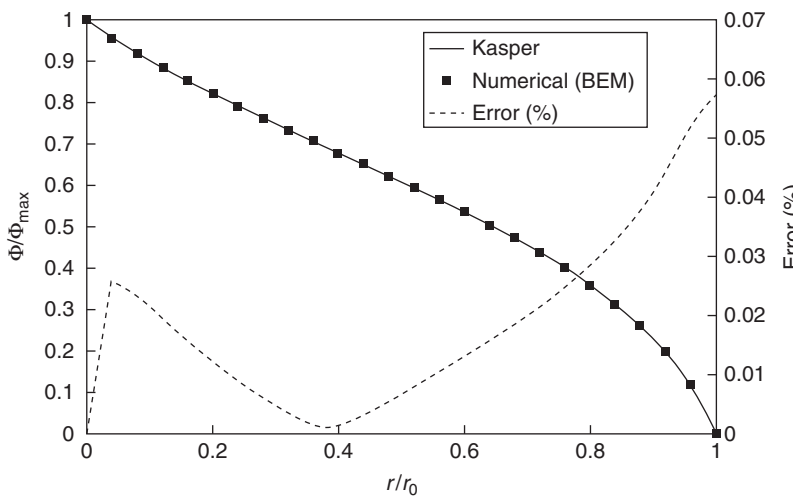

4.5 Comparison of the potential within the electrolyte to Kasper's solution for two parallel cylinders. The variable r/r_0 represents the distance from the edge of the first cylinder normalized to the distance between the cylinders.

4.4.2 Example calculation

To illustrate the manner in which on- and off-potentials are calculated, a simulation was performed for a 1.6 km (1-mile) stretch of pipe. The pipe was connected to a high-performance magnesium anode located at the 0.305 km (1000 ft) position along the length of the pipe. A 0.9×0.3 m^2 (3×1 ft^2)

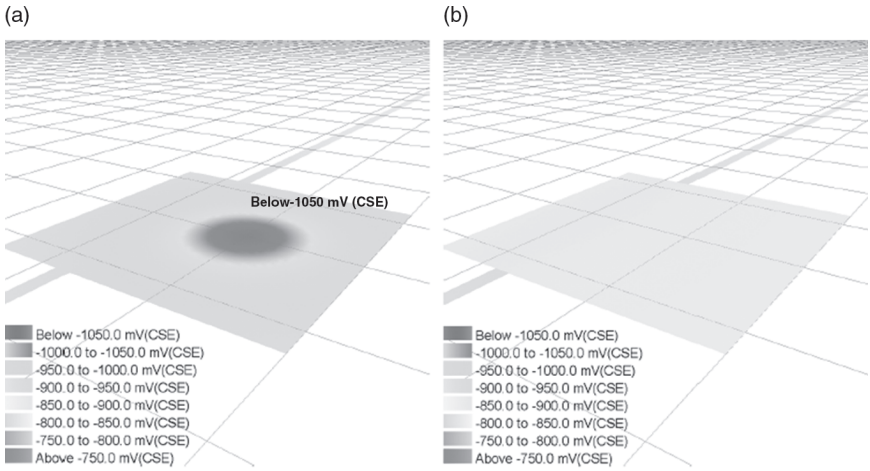

4.6 Calculated potential distribution on the soil surface above the anode (see Fig. 4.7): (a) on-potentials; (b) off-potentials.

coating defect, exposing bare steel, was assumed to be located at the 0.762 km (2500 ft) position. The pipeline was located 0.61 m (2 ft) below grade. Surface on-potentials, shown in Fig. 4.6a, reveal the location of the anode. The grid spacing used in these calculations was 6.1 m × 6.1 m (20 ft × 20 ft). For reference, the corresponding configuration of pipe and anode is presented in Fig. 4.7. As shown in Fig. 4.6b, surface off-potentials, calculated by removing the influence of the anode, obscure the anode location.

The location of a massive ($0.9 \times 0.3\,m^2$) coating defect is seen in the surface on-potentials, shown in Fig. 4.8a, in which the color scale has been changed to facilitate viewing of the potential variation. The significant change in potential at the soil surface level is seen for these calculations because the defect is large, is located at the top of the pipe, is severely under-protected, and is located very close to the soil surface. The values of the off-potential readings shown in Fig. 4.8b suggest that the pipe is under-protected. The size of the coating defect can be seen in Fig. 4.9, where a false-color image of the cathodic current is presented. The majority of CP current is delivered to the exposed steel at the coating defect.

The on- and off-potential distributions shown in Figs 4.8a and 4.8b may be measured in the field, whereas the information presented in Fig. 4.9 could be inferred only after excavation. The BEM model could be used to calculate other measurable quantities, such as the local values for current passed through the pipe. Thus, the BEM model can be used to provide information that can be correlated to the results of ECDA simulations. Such an approach has been suggested for inverse models for interpretation of field ECDA data.[26,27]

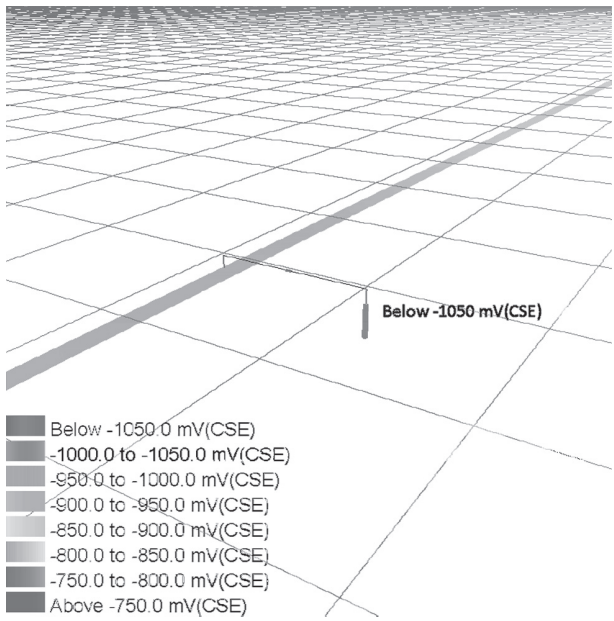

4.7 Image revealing the location of the anode and pipeline corresponding to Fig. 4.6.

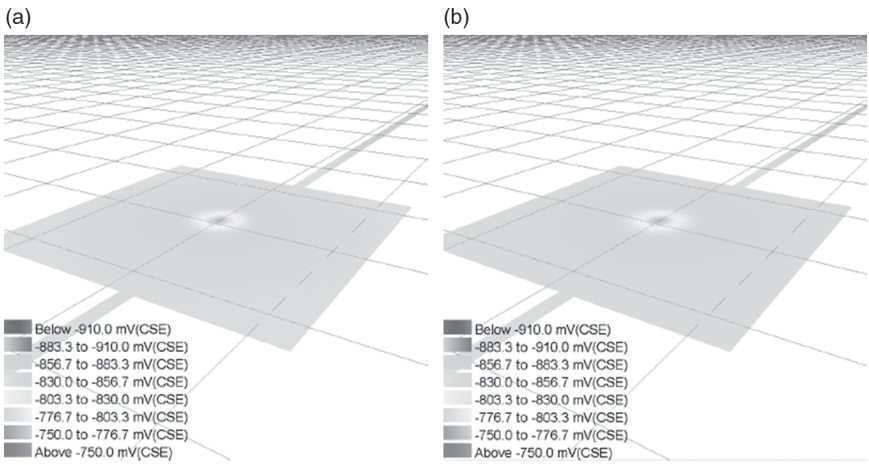

4.8 Calculated potential distribution on the soil surface above a $0.9 \times 0.3\,m^2$ ($3 \times 1\,ft^2$) coating defect exposing bare steel: (a) on-potentials and (b) off-potentials.

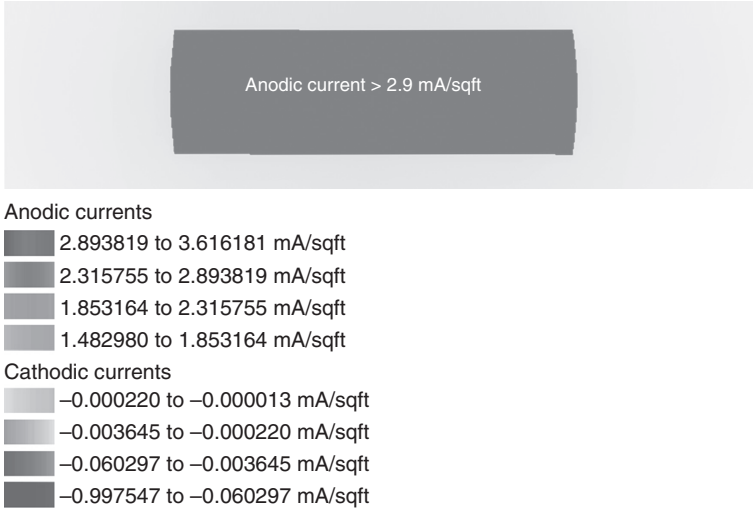

4.9 False-color image of the calculated current distribution on the surface of a coating defect.

4.5 Applications

Three applications of CP models are presented in this section. The model is used to provide guidance for assessing the condition of the buried pipes through indirect techniques based on currents and potentials measured at the soil surface. In a second example, the model is used to demonstrate the coupling between individual CP systems associated with rectifier wars. In a third example, the model is used to explore the role of coatings on protection of tank bottoms.

4.5.1 Simulations for external corrosion direct assessment (ECDA)

Indirect techniques based on currents and potentials measured at the soil surface can be used to evaluate the condition of buried pipelines. These techniques are the foundation of ECDA protocols.[28] The CP model was used to generate simulations to explore the sensitivity of close interval survey (CIS), direct current voltage gradient (DCVG), alternating current voltage gradient (ACVG), and current attenuation techniques to pipe condition.

Calculations were performed for a 16.1 km (10 mile) stretch of pipe with model parameters as listed in Table 4.1. The pipe was protected for all simulations by an impressed current CP system. The anode was located at

Table 4.1 The matrix of model runs showing the ranges of different parameters that were varied

Flaw size in^2 (cm^2)	Soil resistivity kΩ cm	Depth of cover ft (m)	Pipe outside diameter in (cm)	CP level mV(Cu/$CuSO_4$)
1 (6.5)	0.5	4 (1.22)	6 (15.2)	–799 to –700 (low CP)
16 (103)	3	8 (2.44)	12 (30.5)	–999 to –900 (med CP)
36 (232)	10	16 (4.88)	48 (122)	–1199 to –1100 (high CP)
64 (413)	50			
100 (645)	100			
	1000			

3.5 km (11 500 ft) along the length of the pipe and was placed at a depth of 1.6 km (5250 ft). The coating defect was located at 7.92 km (26 000 ft) along the length of the pipe and was placed on the top surface of the pipeline. The pipeline was located 1.21 m (4 ft) below grade. The surface potentials presented are those in close proximity of the coating defect and represent over-the-line potentials.

Soil surface potentials, calculated for a line directly above the pipe and in close proximity to a large coating flaw, are presented in Fig. 4.10. These results were generated from the mathematical model described in Section 4.3 and were intended to mimic CIS results. The nodes of the soil surface that lie directly above the pipeline were spaced 0.61 m (2 ft) apart. The smaller measurement intervals were used to improve resolution of the profiles generated. Normally, the CIS measurements are taken at intervals between 0.75 m (2.5 ft) to 1.5 m (5 ft). A dip is present for both the on-potential profile and the off-potential profile. The dips in potential are caused by the local large values of cathodic current densities associated with the coating flaw. The locally large value of current density creates a corresponding potential distribution at the soil surface. The on-potentials are more negative and at more protected potentials than the off-potentials, due to the CP system being connected for on-potential measurements and disconnected for off-potential measurements. Figure 4.10 provides a typical soil surface potential profile expected for a single coating defect. The influence of coating flaw size on the surface potential readings is presented in Fig. 4.11. The magnitude of the size of the dips increases with increasing coating defect size.

The influence of soil resistivity on the surface potential readings is presented in Fig. 4.12. As soil resistivity increased, the on-potential became more positive, indicating that the CP system's protection of the pipeline has decreased. This is due to a reduced amount of current that can reach the pipeline at higher soil resistivities. No trend was found relating the size of the dips with changes in soil resistivity. The off-potential profiles were

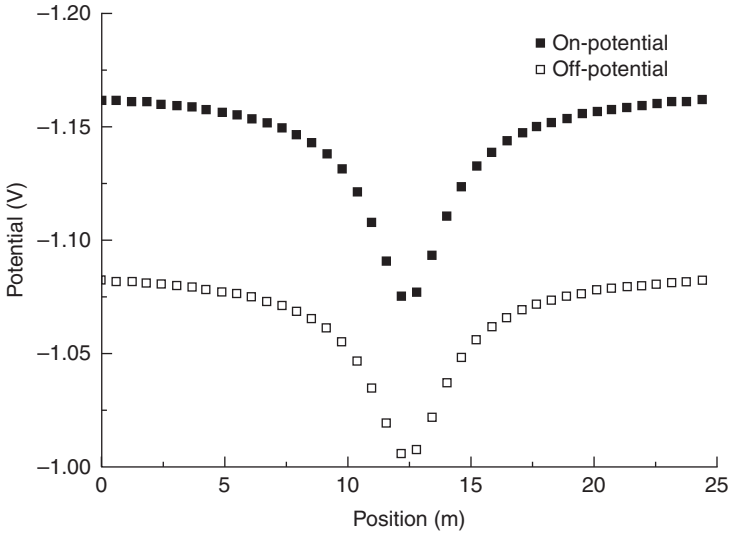

4.10 CIS data generated by the mathematical model in the proximity of a coating defect. The coating defect size was 645 cm^2 (100 in^2) and was placed at a position 12.5 m along the length of the soil surface.

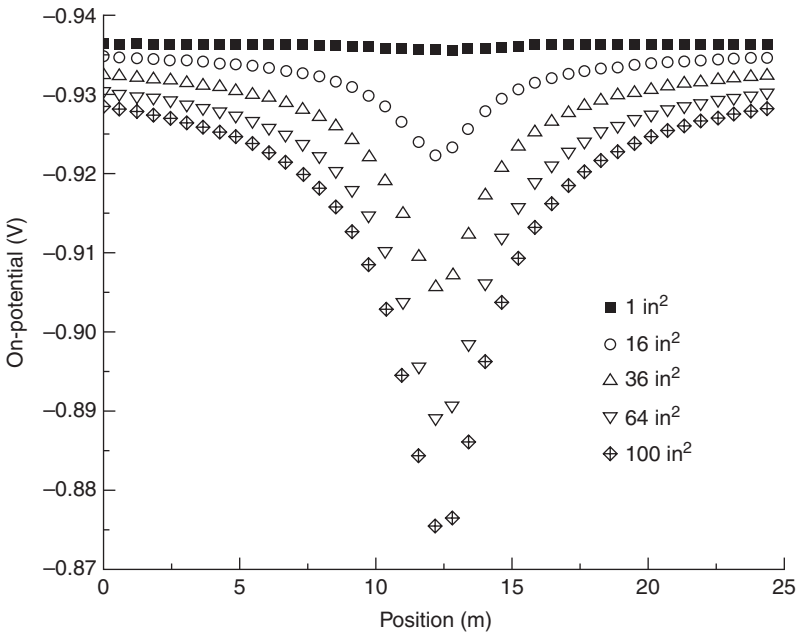

4.11 The over-the-line soil surface on-potentials as a function of position along the soil surface with coating defect size as a parameter.

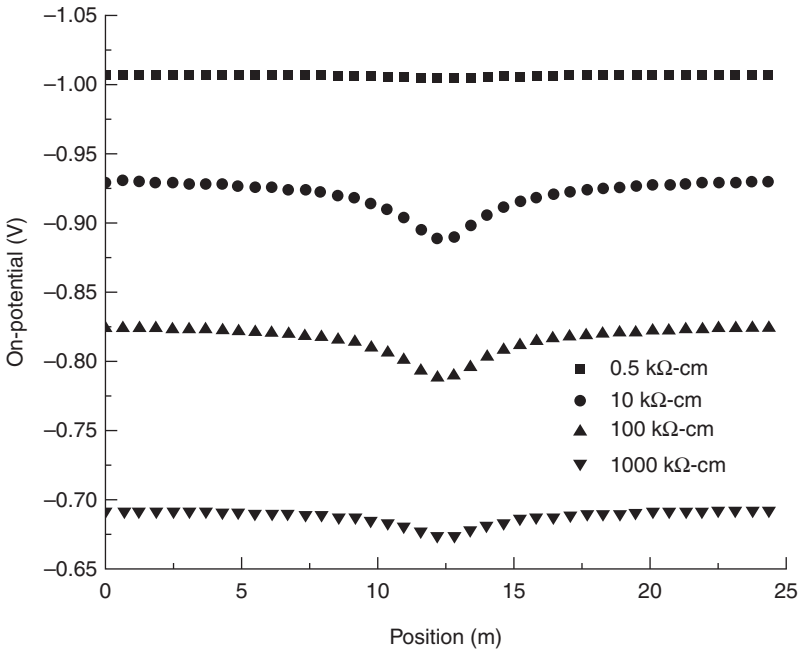

4.12 The over-the-line soil surface on-potentials as a function of position along the soil surface with soil resistivity as a parameter.

then subtracted from the on-potential profiles and are presented in Fig. 4.13. Figure 4.13 demonstrates that the difference in the on- and off-potentials also yields a dip centered at the location of the coating defect. The simulation results show that dips become smaller as soil resistivity increases. For soil resistivity values of 100 kΩ and above, no dips in potential were present, suggesting that high soil resistivities may hide the presence of a coating flaw.

The effect of soil resistivity and coating flaw (holiday) size on the value of calculated indications was first explored using software utilizing Section 4.3. Figure 4.14 was developed to show the correlation between DCVG indications in mV versus flaw size based on changing soil resistivities. Two main trends are found in Fig. 4.14. One trend is that DCVG indications in mV will increase with increasing flaw size, which is consistent with conventional knowledge. The other trend is that as soil resistivity increases the DCVG indication decreases. This trend is a result that was not initially expected. Since these are competing trends, it is of interest to determine which trend has a dominating effect on indications. By taking a closer look at Fig. 4.14, it appears that soil resistivity plays a larger role than flaw size in determining DCVG indication in mV. This is supported by the behavior

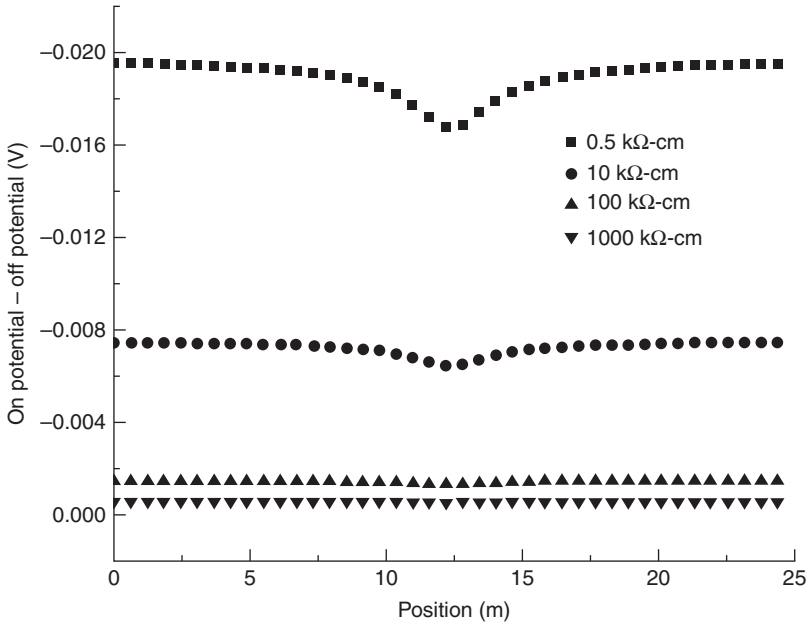

4.13 The difference in on- and off-potentials as a function of position along the soil surface with soil resistivity as a parameter.

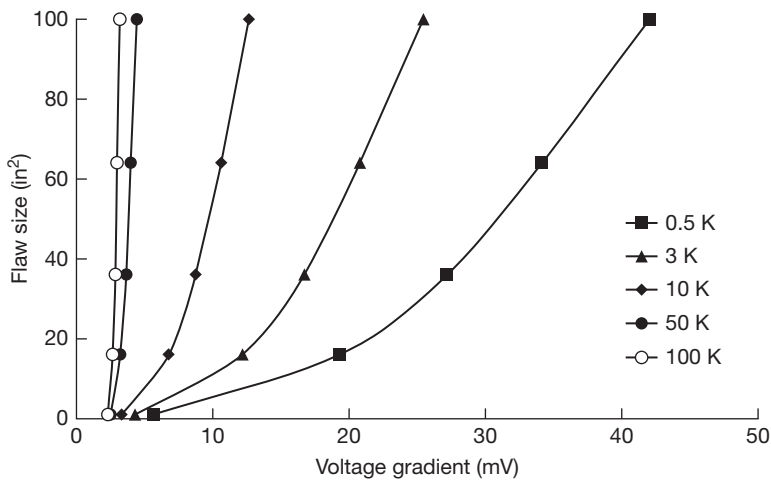

4.14 Coating flaw size as a function of the DCVG indication in mV with soil resistivity as a parameter. The pipe diameter was 12 in, the depth of cover was 4 ft, and the anode potential was 5 V.

at high soil resistivities, where the DCVG indications show almost no dependence on flaw size. Conversely, there is a wide distribution of DCVG indications at low soil resistivities. This result shows that prioritization of DCVG indications in mV can be much improved by taking soil resistivity into account.

DCVG indications were converted to percent-IR, as shown in Fig. 4.15. This plot also shows the effect of soil resistivity and flaw size on indications, except that here the DCVG indications are in percent-IR. In this case, the percent-IR calculations were made by scaling by the IR drop over the coating flaw. The results show that percent-IR indication increases both with increasing coating flaw size and increasing soil resistivity. This plot also shows that soil resistivity can have a greater effect on percent-IR values than flaw size. For example, for each soil resistivity, the relative change of indications stays the same. This means that as flaw size changes, the percent-IR indication changes by the exact same incremental value regardless of what soil resistivity that the system is at. This result shows that percent-IR indications can also be better prioritized by taking soil resistivity into account. In other words, the percent-IR indications obtained could be misinterpreted, causing an inaccurate prediction of the coating flaw severity if the soil resistivity is not known or included in evaluations. For example, in Fig. 4.15, a large percent-IR value could be due to a high soil resistivity and not necessarily a large coating flaw size.

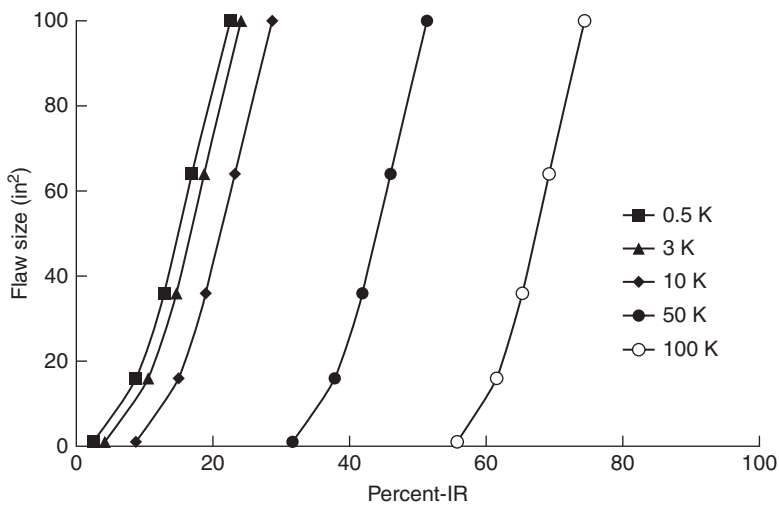

4.15 Coating flaw size as a function of the DCVG indication in percent-IR with soil resistivity as a parameter. The pipe diameter was 12 in, the depth of cover was 4 ft, and the anode potential was 5 V.

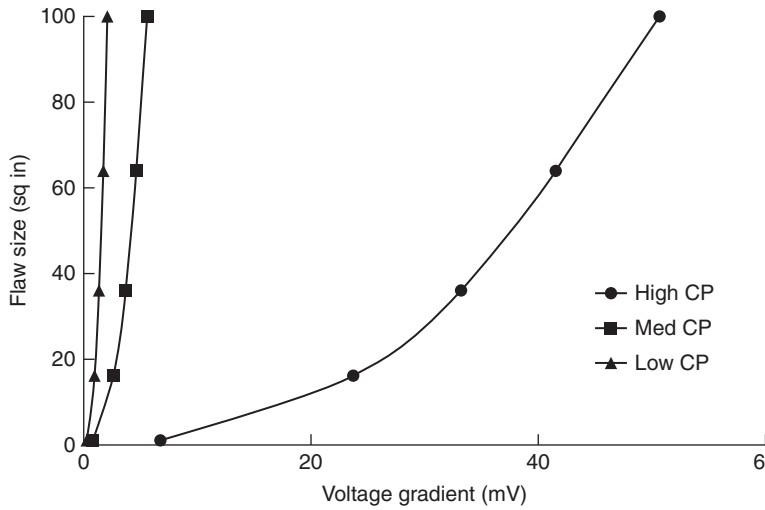

4.16 Coating flaw size as a function of the DCVG indication in mV with CP level as a parameter. The pipe diameter was 12 in, the depth of cover was 4 ft, and the soil resistivity was 500 Ω cm.

In Fig. 4.16, the effect of changing CP levels is explored on DCVG indications in mV. The CP level was adjusted by increasing the anode voltage, and CP levels were categorized by ensuring that off-potentials on the soil surface far away from the coating flaw were within certain ranges. The CP levels and their corresponding potential ranges are shown in Table 4.1. Figure 4.16 also shows that DCVG indications increase with increasing coating flaw size as previously found. However, this graph is primarily included to show that increased CP has a large effect on DCVG signal in mV. Notice that the distribution in voltage gradients in Fig. 4.16 is more apparent at larger CP levels. These larger voltage gradients at higher CP levels can be explained by a larger amount of current entering the pipeline at the flaw location. This shows that at lower CP levels, the presence of a flaw size could be undetected. Therefore, the severity of a flaw could be misinterpreted if CP levels were not taken into account. A sufficient amount of CP current is needed in order to yield a measurable voltage gradient. DCVG in percent-IR was also plotted exactly as in Fig. 4.16. This is shown in Fig. 4.17. The obvious result shown here is that the percent-IR values do not change with increased CP level. This result could be helpful in predicting flaw size based on DCVG indications in percent-IR.

Sensitivity of indications of DCVG in mV is also evaluated based on changing depth of cover as shown in Fig. 4.18. The results show that DCVG indications are more sensitive to a pipeline buried at 4 ft than at 8 ft. Although not shown here, previous simulations have further supported

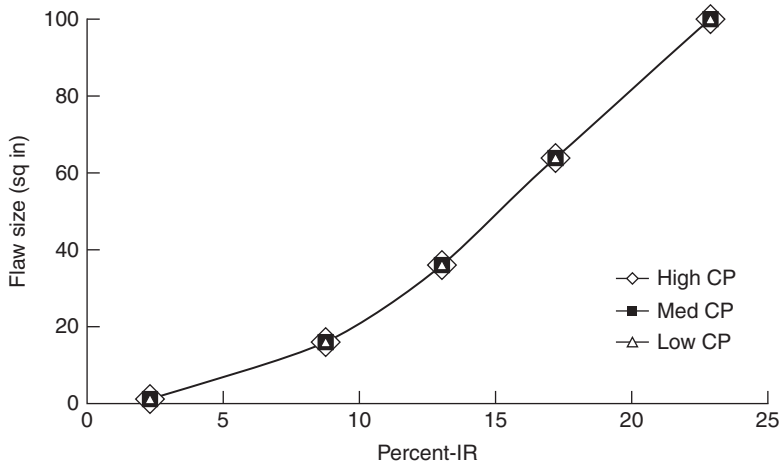

4.17 Coating flaw size as a function of the DCVG indication in percent-IR with CP level as a parameter. The pipe diameter was 12 in, the depth of cover was 4 ft, and the anode potential was 5 V. The pipe diameter was 12 in, the depth of cover was 4 ft, and the soil resistivity was 500 Ω cm.

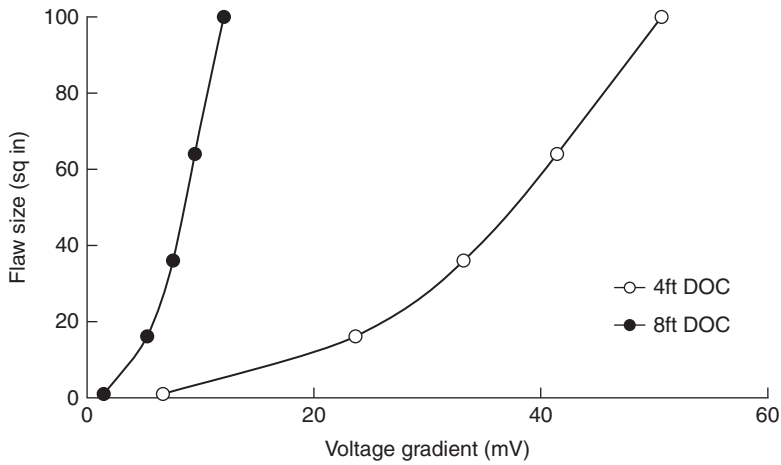

4.18 Coating flaw size as a function of the DCVG indication in mV with depth of cover (DOC) as a parameter. The pipe diameter was 12 in, the soil resistivity was 500 Ω cm, and the CP level was high.

this trend where indications at larger depths of cover are practically negligible. This trend indicates that depth of cover should be used in prioritizing indications. For similar conditions in Fig. 4.18, a plot of DCVG indication in mV is given versus changing pipe diameter. There is no clear trend found

from this result, as shown in Fig. 4.19. However, this result is not considered as proof that pipe diameter does not have an effect on DCVG indication in mV.

CIS on-potential dip (on-dip) indications are plotted against flaw size based on changing soil resistivity in Fig. 4.20. One basic trend shows that

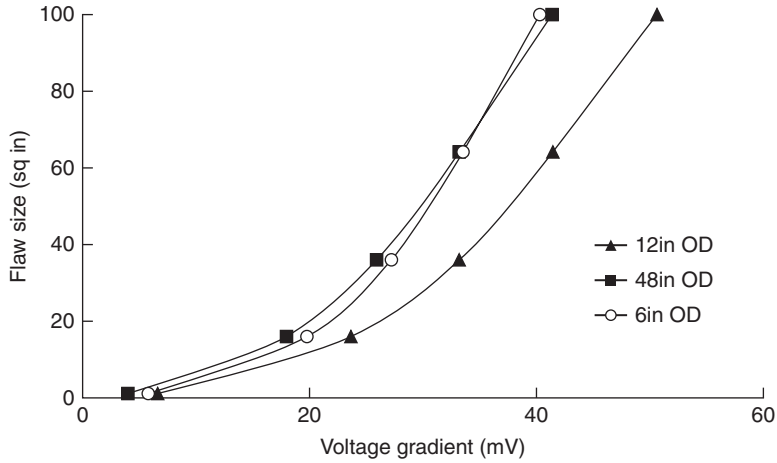

4.19 Coating flaw size as a function of the DCVG indication in mV with pipe diameter (OD) as a parameter. The soil resistivity was 500 Ω cm, the DOC was 4 ft, and the CP level was high.

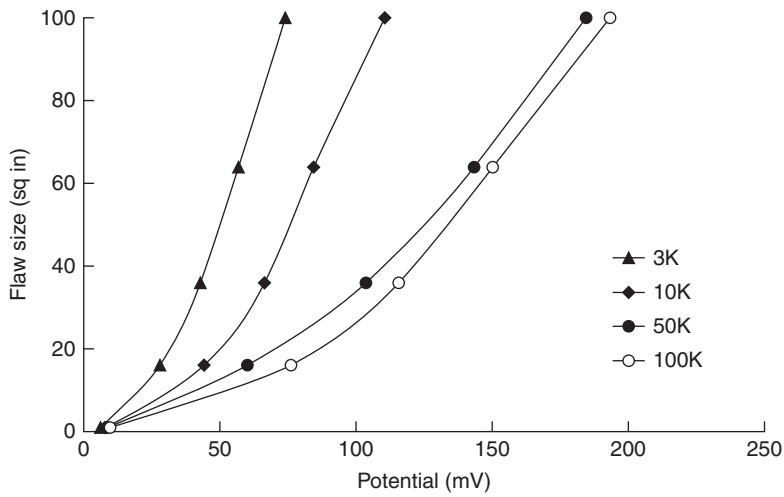

4.20 Coating flaw size as a function of the CIS on-potential dip indication in mV with soil resistivity in Ω cm as a parameter. The pipe diameter was 12 in, the DOC was 4 ft, and the CP level was high.

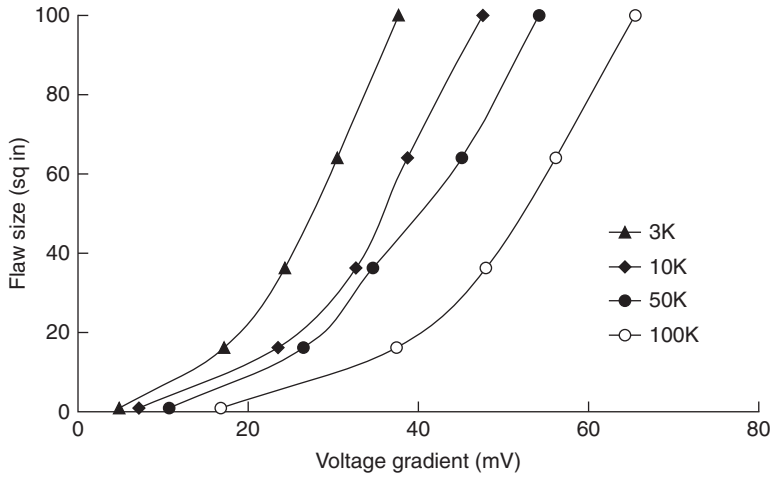

4.21 Coating flaw size as a function of the DCVG indication in mV with soil resistivity in Ω cm as a parameter. The pipe diameter was 12 in, the DOC was 4 ft, and the CP level was high.

CIS on-dip indication increases with increasing flaw (holiday) size. Another trend is that the CIS on-dips increase as soil resistivity increases. However, this result is due to increasing the anode voltage for higher soil resistivities. The anode voltage was adjusted for each simulation to maintain a high CP level (refer to Table 4.1). If the anode voltage had been held constant throughout all runs, the indications would have decreased with increasing soil resistivity. DCVG indications were also calculated for high CP levels, as shown in Fig. 4.21. Note that the DCVG trend in mV for Fig. 4.21 is opposite with respect to soil resistivity than it was in Fig. 4.14. This is because in Fig. 4.14, the anode voltage was held constant for all runs. This indicates that raising the anode voltage increases the DCVG indication found, even if soil resistivity is simultaneously increased.

Figure 4.22 is based on data from the same simulations run in Fig. 4.20. However, it shows a different result for some soil resistivities. The negative CIS off-dips initially represented an area of concern. The on- and off-potential profiles are given for a simulation that gives a negative CIS off-dip in Fig. 4.23. A general potential profile represents current direction by moving from positive to negative potentials. In Fig. 4.23, the on-potential profile shows that current enters the pipeline at the coating flaw and then travels away from the flaw based on the profile of on-potential moving from positive to negative. This behavior is normally expected for the off-potential profile as well. However, the negative CIS off-dip indicates that when the CP current is turned off, the potential flows back toward the flaw. This can

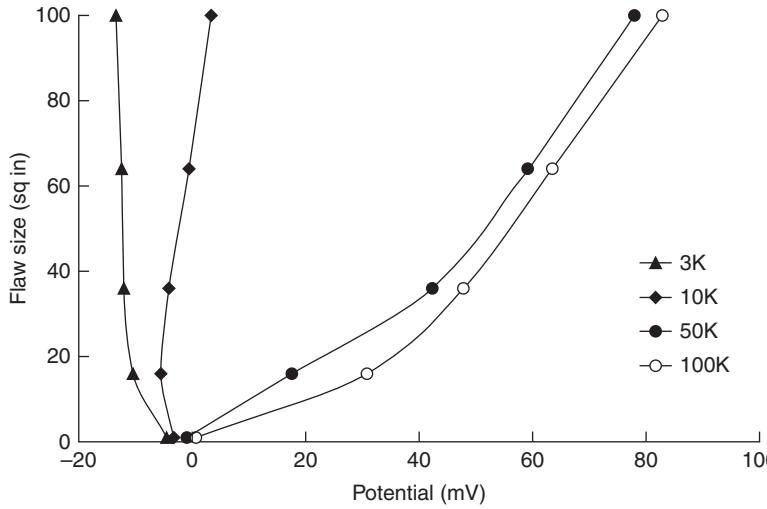

4.22 Coating flaw size as a function of the CIS off-potential dip indication in mV with soil resistivity in Ω cm as a parameter. The pipe diameter was 12 in, the DOC was 4 ft, and the CP level was high.

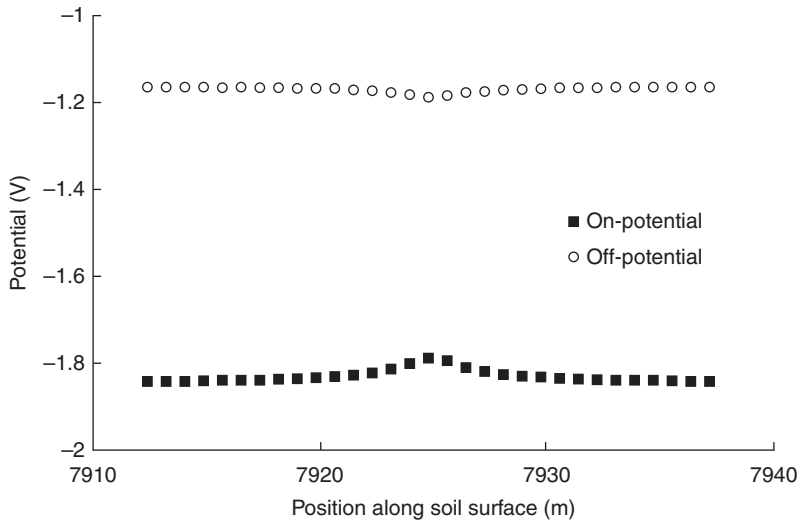

4.23 A profile of soil surface on- and off-potentials from a simulated CIS survey. The flaw size was 36 in^2, the soil resistivity was 500 Ω cm, the pipe diameter was 12 in, the DOC was 4 ft, and the CP level was high.

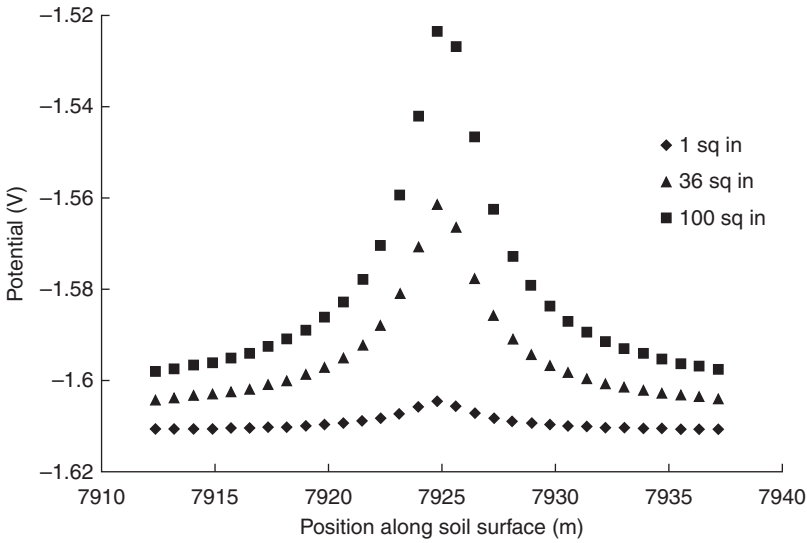

4.24 Soil surface on-potential as a function of position along the length of the pipeline with flaw size as a parameter. The anode voltage was the same for each simulation.

be attributed to the pipeline being substantially over-protected underneath the coating than it is at the flaw. This is explained to occur at low soil resistivities because the coating resistance is so much higher than the resistance of the soil when the soil resistivities are low.

Another way to prioritize CIS indication is to calculate the dips in potential to determine the relative size of the coating. From simulation data it can be shown that the size of the dip has a direct correlation with the size of the flaw. This result is shown in Fig. 4.24. This trend shows that the magnitude of the dip increases with increasing size of the coating flaw.

Coating flaw size predictors

All simulation data results were used to predict flaw size based on CIS indications. The simulation data used involve variation in CP level, pipe diameter, depth of cover, and soil resistivity. A design equation was developed which predicts coating flaw size through use of the CIS dip indications. Figure 4.25 shows all simulation data of CIS indication versus coating flaw size. The CIS indication shown represents the difference in the on-potential dip and the off-potential dip. The on-potential dip is illustrated as Dip_{on} in Fig. 4.26 and the off-potential dip is illustrated as Dip_{off}. Each of the parameters was incorporated into an expression to predict flaw size using a least squares regression method.

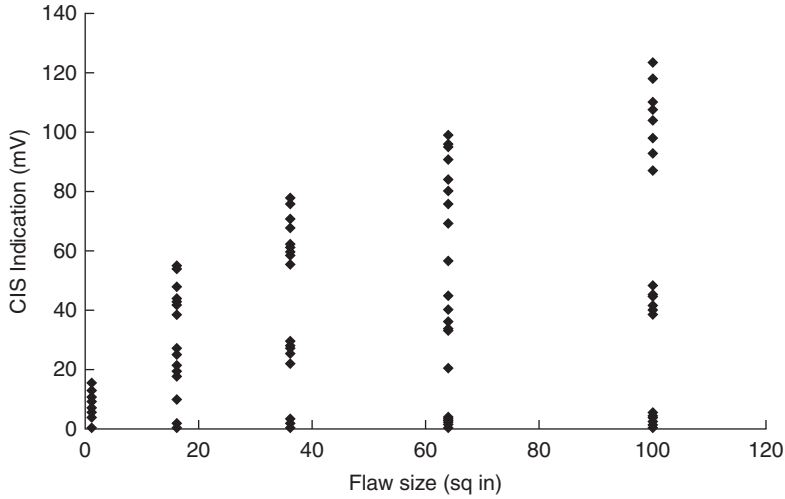

4.25 CIS indications as a function of flaw size obtained from a large set of simulations. The CIS indication is the difference between the on-potential dip and the off-potential dip, as is shown in Fig. 4.26.

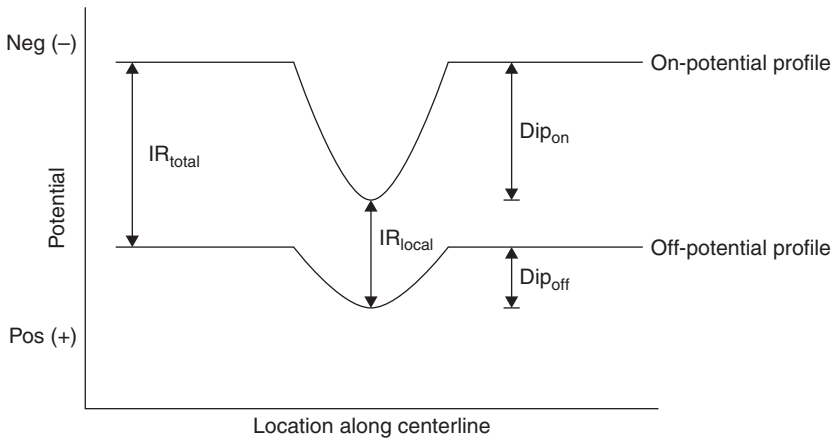

4.26 A profile of on- and off-potentials along the centerline at the soil surface.

Once the expressions for the different parameters are lumped together, a value for flaw size can be predicted within a calculated confidence interval for a given simulation. This is used to show that the CIS predictor is not predicting an exact coating flaw size, but instead a range within which the true coating flaw size should be. For each simulation run, the corresponding flaw size was predicted. A plot of actual flaw size versus predicted flaw size

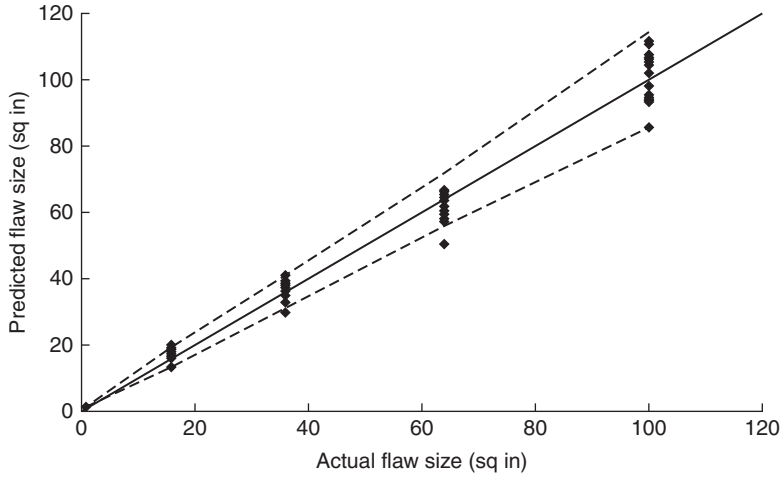

4.27 Input flaw size as a function of predicted flaw size for each simulation using CIS indications.

is shown in Fig. 4.27. Good agreement is shown in the graph, evidenced by a high R^2 value of 0.986. The calculated confidence interval is represented by the dashed lines. In order for the coating flaw size to be predicted, the soil resistivity and depth of cover must be known. Then by using CIS on- and off-dip indications, as well as the IR total value illustrated in Fig. 4.26, the flaw size can be predicted. Changes in CP levels or in the size of the pipe diameter showed no effects on the prediction of flaw size using CIS indications.

Similar development was used to predict flaw size based on DCVG indications. A separate design equation was created from this development. While the CIS predictor was based on IR drops far away from the coating flaw but along the pipeline, the DCVG predictor used IR drops far away from the coating flaw but in the direction perpendicular to the pipeline. The IR drops used in calculating percent-IR include the DCVG indication survey data needed for the predictor. For the predicted flaw size to be calculated, the soil resistivity, depth of cover, and pipe diameter must also be known. In Fig. 4.28, the agreement between predicted flaw size and actual flaw size is shown. The confidence interval for the predicted flaw size is also given by the dashed lines.

Assessment of poor coatings

Additional simulations were run to improve assessments of coatings that are in bad condition. Coatings with lower resistivities (i.e. 10^6 Ω-cm) are considered to be in poor condition. All results of this work in previous sections

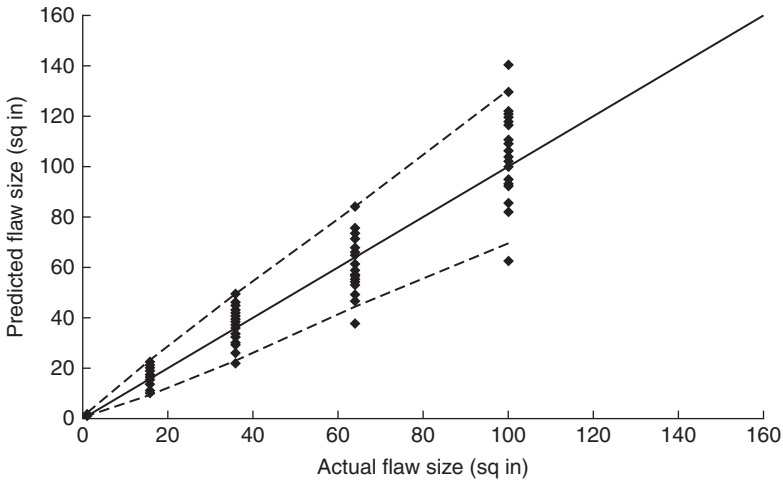

4.28 Input flaw size as a function of predicted flaw size for each simulation using DCVG indications.

have been based on detecting a coating flaw. However, this section focuses on determining if the overall coating is in bad condition. This primarily aims at helping field engineers differentiate between the conditions favorable for pipeline failure by either large continuous sections of bad coating or by a local coating flaw.

The first set of simulations involved a pipeline without a coating versus a pipeline with a good coating (i.e. 10^9 Ω-cm). The pipeline without a coating was specified as aged bare steel. The simulations with a coating had properties corresponding to that of 20 mil fusion bonded epoxy (FBE). Variations in soil resistivity, pipe diameter, depth of cover, and CP level were done by performing numerous simulations.

From these simulation results, the soil surface potentials along the centerline for each simulation run were uniform. This is because the condition of the pipeline was uniform and there was no localized current entering the pipeline due to the absence of an isolated coating flaw. The soil surface potentials were further explored in the direction perpendicular to the pipeline. The soil surface potentials were not uniform moving away from the pipeline for the aged bare steel, but they were relatively uniform for the coated pipeline. For the aged bare steel, it was found that the potential drop was not a function of position in respect to the length of the pipeline. This means that a lateral voltage gradient would be the same at any position along the pipeline, assuming it was located at the same distance away from the pipeline. In all simulations, CIS and DCVG indications in mV gave no results, due to the lack of localized current flow to a coating defect.

However, due to the potential drop moving away from the pipeline in the bare steel simulations, percent-IR calculations could be done. The lengthwise position of the percent-IR calculation was done near the center of the pipeline to be consistent with calculations of percent-IR in previous sections. However, this location is arbitrary, since potential drops were found to not change with position along the length of the pipeline. The percent-IR results showed no substantial changes with respect to variations in soil resistivity, depth of cover, pipe diameter, and oxygen blocking. It was found that ranges in percent-IR for the aged bare steel were between 65% and 85%, while the percent-IR values were all near zero for that of the 20 mil FBE coating. These results can be attributed to a large amount of current entering the pipeline for the aged bare steel due to a larger current demand to maintain the pipeline's integrity. Since a minimal amount of current was needed to protect the coated pipeline, the overall soil surface potential distribution was uniform.

Another set of simulations was performed for a pipeline with a poor coating. The coating resistivity was lowered to be equal to that of the soil resistivity. Other properties of the coating were studied, such as oxygen blocking and pore size. Percent-IR calculations found that variations in both of these parameters had no influence, since the percent-IR values were the same for each simulation run. Variations in soil resistivity and CP level all yielded the same percent-IR values. This result showed that percent-IR is insensitive to the amount of oxygen penetrating the coating.

For the final set of simulations, the oxygen blocking level and the pore size were held constant. Coating resistivity was the main parameter being varied from 10^6 Ω-cm to 10^9 Ω-cm. Soil resistivity and CP level were also varied. The percent-IR was calculated for each simulation. A relationship was found by plotting the logarithm of the ratio of coating resistivity to soil resistivity versus percent-IR. This result is shown in Fig. 4.29. The shape of data in Fig. 4.29 resembles the curve of a rotated sigmoid function. The sigmoid function with some slight modification is given as

$$P = \frac{1}{A + \exp(Bx + C)} \qquad [4.30]$$

where P represents percent-IR and x represents the logarithm of the ratio of the coating resistivity to the soil resistivity. Parameters A, B and C were adjusted to fit the function to the simulation data. The equation is rearranged for a rotated sigmoid function as

$$x = -\frac{\ln(P + 0.0124) - 12}{2.325} \qquad [4.31]$$

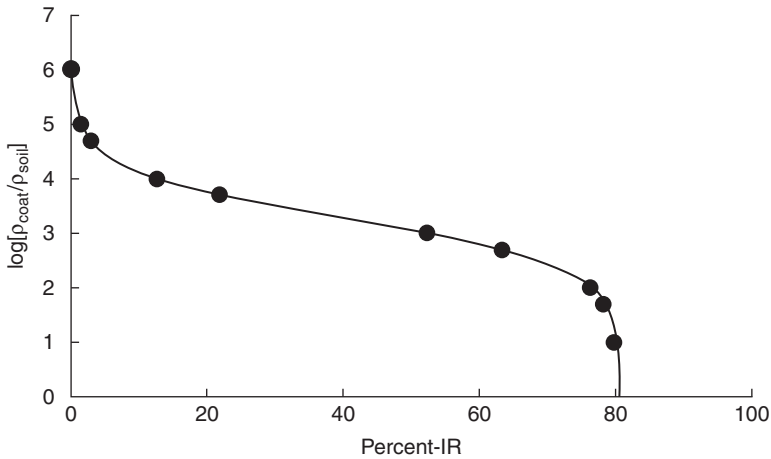

4.29 The logarithm of the ratio of coating and soil resistivity as a function of the percent-IR resulting from simulations in which parameters such as coating resistivity, soil resistivity, and CP level were varied. The line represents the model presented as Equation [4.30].

Figure 4.29 shows the simulation data fitted with the sigmoidal function. The agreement is excellent. These results are expected to be able to improve future assessments of a pipeline's coating condition.

Before using the empirical formula given, surveyors should first determine if a coating flaw is present. This can be done by CIS and DCVG surveys. If no evidence of a coating flaw is found, percent-IR measurements can still be made to help make a determination about the overall coating condition of the pipeline. Then the guideline may be followed to make an assessment. This method is recommended if coating conditions are expected to be poor. Also, they should be used after CIS and DCVG surveys have been carried out and no defects have been found. Then the percent-IR calculation can be completed to help make an assessment about the overall coating condition of the pipeline.

4.5.2 Rectifier war

The term 'rectifier war' describes the influence the rectifier for one CP system may have on an adjacent CP system. Increases in the rectifier output for one system may cause corrosion of an adjacent system. The subsequent increase in the rectifier output of that system will cause corrosion of the first system.

Two 1 km long coated pipes in a soil of 10 kΩ cm resistivity were assumed to cross, as shown in Fig. 4.30. The coating on the two pipes had the same

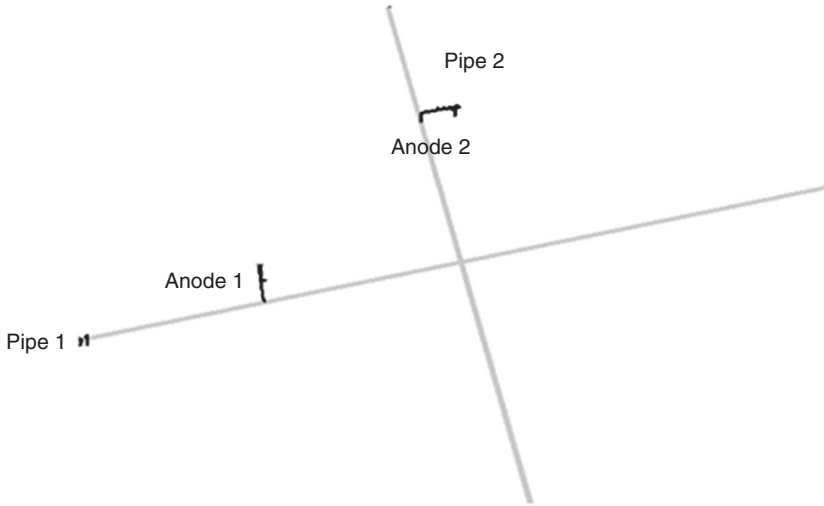

4.30 Configuration of pipes and anodes for the simulation of rectifier wars.

properties, and the pipes experienced the same level of CP at an applied rectifier voltage of 1.35 V. A comparison of the potential and current density distributions on Pipe 1 before and after introducing Pipe 2 is shown in Figs. 4.31 and 4.32 respectively. The valleys that appear in both figures were associated to the site of pipe where anodes were connected. The peaks indicate the interference between two pipes, but the interference was not very strong because the potential difference of the peak is small in Fig. 4.31.

Potential and current density distributions are shown in Figs 4.33 and 4.34, respectively for the case when the rectifier voltage for Pipe 1 was increased to 5.8 V. These two figures indicate that Pipe 1 experienced more CP than did Pipe 2, since the potential and current density distributions along Pipe 1 were more negative than that along Pipe 2. Corrosion begins to occur on the site of Pipe 2 that is associated with the cross-over section. This point can be clearly illustrated by Fig. 4.35, which provides a comparison of potential distributions of Pipe 2 in two conditions. The peak, which was above the –850 mV CSE criterion, referenced to the $Cu/CuSO_4$ electrode (CSE), indicates that the CP difference between the two pipes may result in the localized corrosion at the cross-over section on the pipe, which has less CP.

4.5.3 Tank bottoms

Riemer and Orazem had reported that, for oxygen-saturated soil, a 30.5 m diameter uncoated tank bottom cannot be protected by a deep well remote

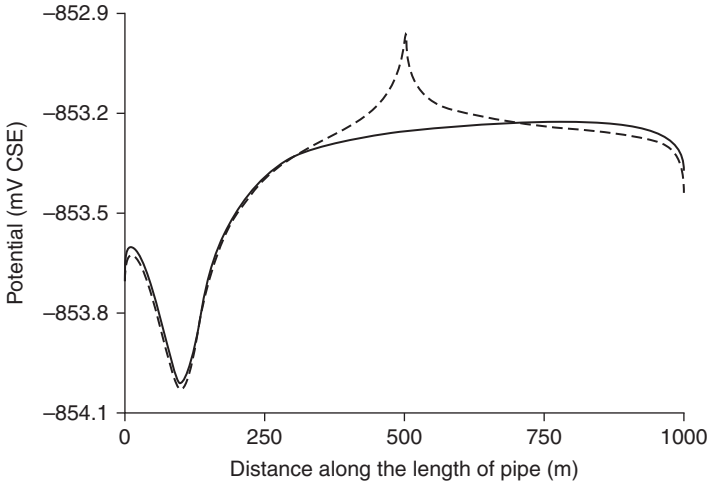

4.31 Comparison of potential distributions along Pipe 1 before and after introducing Pipe 2. Solid line: before introducing Pipe 2; dash line: after introducing Pipe 2.

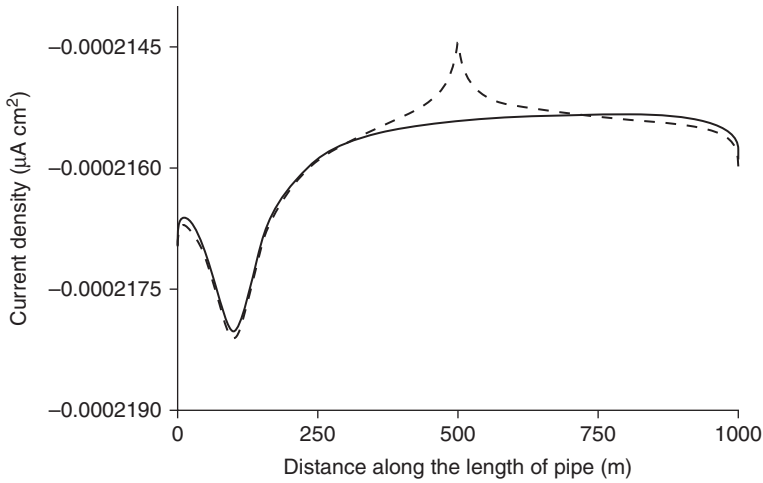

4.32 Comparison of current density distributions along Pipe 1 before and after introducing Pipe 2. Solid line: before introducing Pipe 2; dash line: after introducing Pipe 2.

ground bed located 2000 ft below the tank when the output of the anode is 14.2 A. To explore this observation, and to explore the role of coatings and coating holidays, a series of simulations were performed for a tank diameter of 45.7 m, and a 1m long anode directly below the tank bottom at a distance of 1000 m. The soil was assumed to have a uniform resistivity

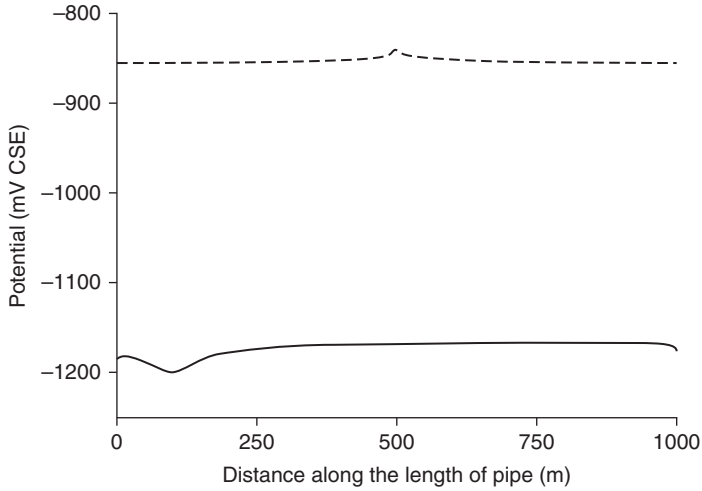

4.33 Comparison of potential distributions along Pipe 1 and Pipe 2 respectively in Condition 2. Solid line: Pipe 1; dash line: Pipe 2.

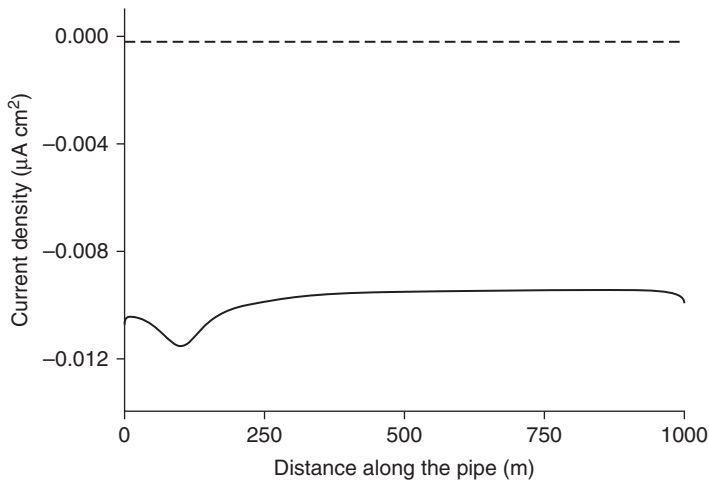

4.34 Comparison of current density distributions along Pipe 1 and Pipe 2 respectively in Condition 1. Solid line: Pipe 1; dash line: Pipe 2.

of 10 kΩ cm. The polarization parameters used are given in Table 4.2. The difference between Steels A and B is that the mass-transfer-limited current density for oxygen reduction was larger for Steel B than for Steel A, and Coating B had greater permeability to oxygen than did Coating A.

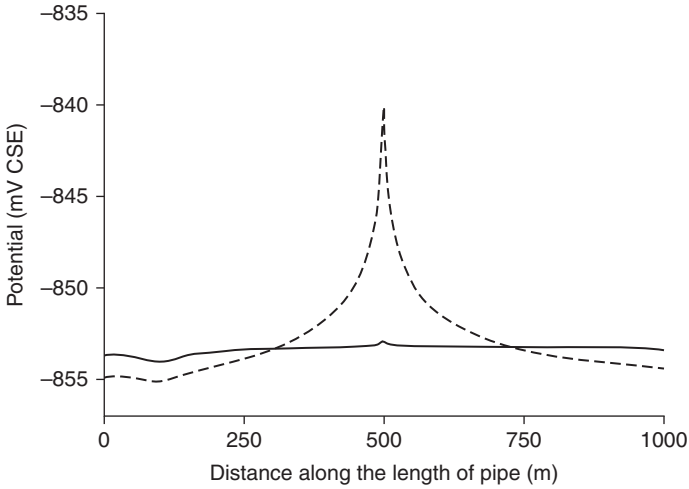

4.35 Potential distributions of Pipe 2 in Conditions 1 and 2, respectively. Solid line: Pipe 2 in Condition 1; dash line: Pipe 2 in Condition 2.

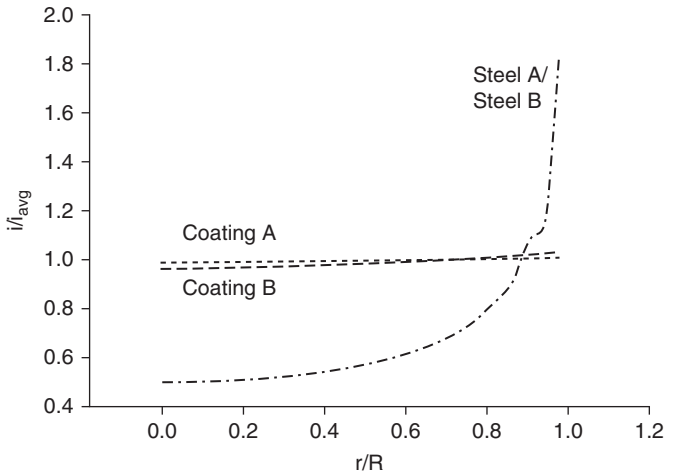

4.36 Calculated normalized current density as a function of dimensionless radius on tank bottoms with different surface properties.

The current distributions corresponding to the four cases are shown in Fig. 4.36, and the corresponding parameter values are presented in Table 4.3. In the case of Steel A and Steel B, where no coatings are present, the protection current distribution is observed to be non-uniform, with the periphery having higher current density than the middle of the tank bottom. By

Table 4.2 Parameters corresponding to tank bottom simulations (see Equations [4.6], [4.9], and [4.10])

Type of coating	Coating A	Coating B	Steel A	Steel B
Coating resistivity ρ, M Ω cm	5000	200	–	–
Coating Thickness δ, mm	0.508	0.508	–	–
Oxygen blocking α_{block}, %	99.9	99	–	–
A_{pore} / A, %	0.1	0.1	–	–
E_{Fe}, mV	–522	–522	–522	–522
β_{Fe} , mV/decade	62.6	62.6	62.6	62.6
i_{lim,O_2}, μA/cm²	1.05	1.05	3.1	10.8
E_{O_2}, mV CSE	–172	–172	–172	–172
β_{O_2}, mV/decade	66.5	66.5	66.5	66.5
E_{H_2},mV CSE	–942	–942	–942	–942
β_{H_2}, mV/decade	132.1	132.1	132.1	132.1

Table 4.3 Tank bottom simulation results

Tank steel/coating	Steel A	Steel B	Coating A	Coating B
Type of anode	ICCP – 4750	ICCP – 15500	Standard potential magnesium	Standard potential magnesium
Potential applied, V CSE	4750	15500	–	–
Output current of anode, A	111.62	364.34	0.0092	0.0118
Cross section area of tank bottom, m²	1641.7	1641.7	1641.7	1641.7

increasing the current output, it was possible to drive potentials to values below –850 mV CSE, as shown in Fig. 4.37. The coated tank bottoms were easily protected by the sacrificial Mg anodes. The current distributions were uniform, and the potentials were well within the protected regime.

Additional simulations were performed for coated tank bottoms with coating flaws that exposed bare steel. The coating defect was located at the center of the tank bottom and, as was done for the previous calculation, the anode was placed at a large distance from the tank. Two configurations were studied: Coating A with Steel B exposed in the center of the tank and Coating B with Steel B exposed, respectively. The coating holiday covered a relatively large 5.5 m² which represented 0.35% of the tank area. The soil resistivity was assumed to be uniform, with a value of 10 kΩ cm. The corresponding current and potential distributions are given in Figs 4.38 and 4.39, respectively.

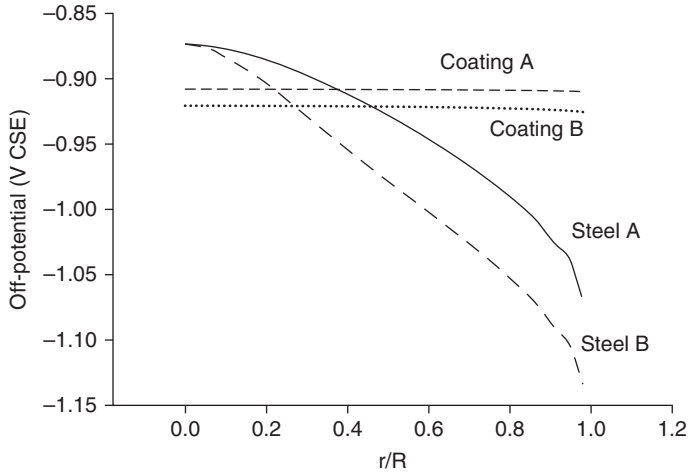

4.37 Calculated off-potential as a function of dimensionless radius corresponding to Fig. 4.36.

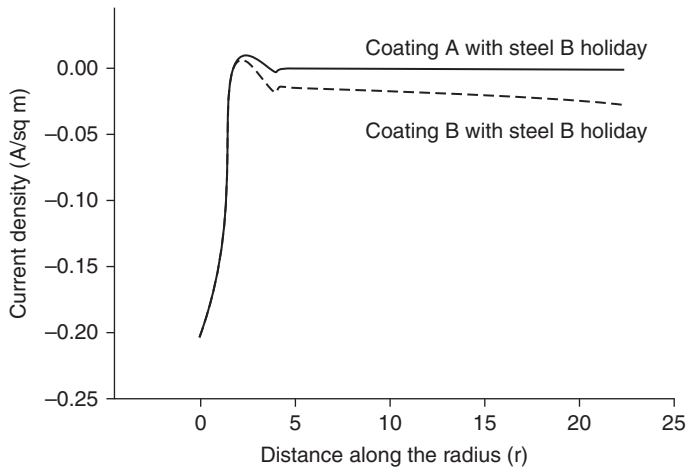

4.38 Calculated current density as a function of radial position for coated tanks with a large coating flaw at the center of the tank.

The coating flaw caused a significant change in the current distribution. The current density was highest at the center of the tank bottom at the defect. To ensure that minimum protection of the entire tank bottom in the case of Coating A was achieved, a large potential of 160 V had to be applied. This resulted in large areas of tank bottom being severely over-protected, as shown by the potential values in Fig. 4.39. In the case of Coating B, a larger potential of 1600 V was applied to ensure that minimum protection was

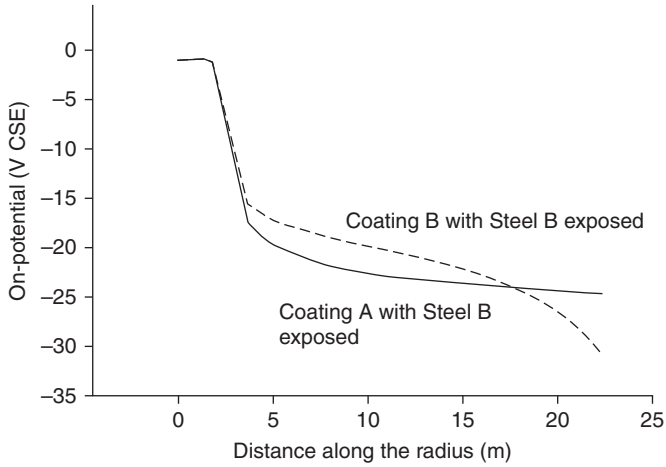

4.39 Calculated on-potentials as a function of radial position corresponding to Fig. 4.38.

achieved for the tank bottom. This also resulted in large areas of the tank bottom being over-protected, as shown by the potential values in Fig. 4.39.

4.6 Conclusion

Numerical simulations are a powerful aid to understanding the nature of CP of buried structures. The ability to calculate on- and off-potentials for surfaces facilitates interpretation of ECDA measurements to assess the condition of buried pipes. The ability to model the interactions between buried structures, and even independent CP systems, becomes important as the number of pipes placed within a right-of-way increases. The model may be applied as well to planar structures, such as the bottoms of storage tanks.

4.7 References

1. A.W. Peabody (1967), *Control of Pipeline Corrosion* (Houston, TX: NACE International).
2. L. Benedict (editor) (1986), *Classic Papers and Reviews on Anode Resistance Fundamentals and Applications* (Houston, TX: NACE International).
3. J. S. Newman (1991), Cathodic protection with parallel cylinders, *Journal of the Electrochemical Society*, **138**, 3554–3560.
4. M. E. Orazem, D. P. Riemer, C. Qiu and K. Allahar (2004), 'Computer simulations for cathodic protection of pipelines,' in *Corrosion Modeling for Assessing the Condition of Oil and Gas Pipelines*, F. King and J. Beavers (editors) (Houston, Texas: NACE International), 25–52.
5. C. A. Brebbia and J. Dominguez (1977), Boundary element methods for potential problems, *Applied Mathematical Modelling*, **1**, 371–378.

6. S. Aoki, K. Kishimoto and M. Sakata (1985), Boundary element analysis of galvanic corrosion, in *Boundary Elements VII*, C. A. Brebbia and G. Maier (editors) (Heidelberg: Springer-Verlag), 73–83.
7. J. C. F. Telles, L. C. Wrobel, W. J. Mansur and J. P. S. Azevedo (1985), Boundary elements for cathodic protection problems, in *Boundary Elements VII*, C. A. Brebbia and G. Maier (editors) (Heidelberg: Springer-Verlag), 63–71.
8. N.G. Zamani and J.M Chuang (1987), Optimal-control of current in a cathodic protection system – a numerical investigation, *Optimal Control Applications & Methods*, **8**, 339–350.
9. F. Brichau and J. Deconinck (1994), A numerical-model for cathodic protection of buried pipes, *Corrosion*, **50**, 39–49.
10. F. Brichau, J. Deconinck and T. Driesens (1996), Modeling of underground cathodic protection stray currents, *Corrosion*, **52**, 480–488.
11. S. Aoki and K. Amaya (1997), Optimization of Cathodic Protection System by BEM, *Engineering Analysis with Boundary Elements*, **19**, 147–156.
12. S. Aoki, K. Amaya and M. Miyasaka (1999), Boundary element analysis of cathodic protection for complicated structures, in Proceedings of the NACE99 Topical Research Symposium: Cathodic Protection: Modeling and Experiment, M. E. Orazem (editor),(Houston, TX: NACE International), 45–65.
13. K. J. Kennelley, L. Bone and M. E. Orazem (1993), Current and potential distribution on a coated pipeline with holidays:1. model and experimental verification, *Corrosion*, **49**, 199–210.
14. M. E. Orazem, K. J. Kennelley and L. Bone (1993), Current and potential distribution on a coated pipeline with holidays:2. a comparison of the effects of discrete and distributed holidays, *Corrosion*, **49**, 211–219.
15. M. E. Orazem, J. M. Esteban, K. J. Kennelley and R. M. Degerstedt (1997), Mathematical models for cathodic protection of an underground pipeline with coating holidays: 1. theoretical development, *Corrosion*, **53**, 264–272.
16. M. E. Orazem, J. M. Esteban, K. J. Kennelley and R. M. Degerstedt (1997), Mathematical models for cathodic protection of an underground pipeline with coating holidays: 2. case studies of parallel anode CP systems, *Corrosion*, **53**, 427–436.
17. D. P. Riemer and M. E. Orazem (2005), Modeling coating flaws with nonlinear polarization curves for long pipelines, in *Corrosion and Boundary Element Methods*, R. A. Adey (editor) (Southampton, UK: WIT Press), 225–259.
18. D. P. Riemer and M. E. Orazem (2000), Application of boundary element models to predict effectiveness of coupons for assessing cathodic protection of buried structures, *Corrosion*, **56**, 794–800.
19. D. P. Riemer and M. E. Orazem (2005), A mathematical model for the cathodic protection of tank bottoms, *Corrosion Science*, **47**, 849–868.
20. J. F. Yan, S. N. R. Pakalapati, T. V. Nguyen, R. E. White and R. B. Griffin (1992), Mathematical modeling of cathodic protection using the boundary element method with a nonlinear polarization curve, *Journal of the Electrochemical Society*, **139**, 1932–1936.
21. D. P. Riemer (2000), *Modeling Cathodic Protection for Pipeline Networks*, PhD dissertation, University of Florida, Gainesville, Florida.
22. C. A. Brebbia, J. C. F. Telles and L. C.Wrobel (1984), *Boundary Element Techniques*, (Heidelberg: Springer-Verlag).

23. I. Stakgold (1979), *Greens Functions and Boundary Value Problems* (New York: John Wiley & Sons).
24. J. Newman (1966), 'Resistance for flow of current to a disk', *Journal of the Electrochemical Society*, **113** 501.
25. C. Kasper (1940), The theory of the potential and the technical practice of electrodeposition: IV. The flow between and to circular cylinders', *Transactions of the Electrochemical Society*, **78** 147–161.
26. J. P. McKinney, M. E. Orazem, O. Moghissi and D. D'Zurko (2006), Development of ECDA criteria for prioritization of indications, Proceedings of Corrosion/2006 (Houston, Texas: NACE International), Paper 06–188.
27. J. P. McKinney, M. E. Orazem, O. Moghissi and D. D'Zurko (2009), Predicting coating holiday size using ECDA survey data, Proceedings of Corrosion/2009 (Houston, Texas: NACE International), Paper 09–146.
28. O. C. Moghissi, W. Harper, M. Celinski, V. Sottile and D. DiMeo (2004), 'External corrosion direct assessment validation through correlation between indications and control excavations', Proceedings of Corrosion /2004 (Houston, Texas: NACE International), Paper 04–187.